Journal of Applied Fluid Mechanics, Vol. 16, No. 12, pp. 2438-2458, 2023.
Available online at www.jafmonline.net, ISSN 1735-3572, EISSN 1735-3645.
https://doi.org/10.47176/jafm.16.12.2029

Thermal–Solid Interaction Study of Serpentine Nozzle and Analysis on Structural Response Law

J. L. Cheng†, S. Huang, and L. Zhou

Shaanxi Key Laboratory of Internal Aerodynamics in Aero-Engine, School of Power and Energy, Northwestern Polytechnical University, Xi'an, 710072, People's Republic of China

†*Corresponding Author Email: 18326066592@mail.nwpu.edu.cn*

ABSTRACT

The serpentine nozzle effectively suppresses infrared radiation and radar signals from advanced aero-engine exhaust system. However, the extreme operating environment of thermal–solid interaction complicates the heat transfer of the flow inside the serpentine nozzle and the structural response of the nozzle itself. In this study, the internal flow heat transfer and the structural response of the serpentine nozzle were investigated numerically. Further, the parameter influence law of wall thickness was explored. The results show that the mechanism of the thermal-solid interaction is formed through the data transfer of the heat flux and the temperature at the interface between the flow field and structure field. The heat flux distribution of the nozzle under the bending configuration is non-uniform. The upper wall surface at the first bend and the lower wall surface at the second bend exhibit the highest heat flux. In the structural response, the temperature extremes appear on the upper wall at the first bend and the lower wall at the second bend. Subsequently, they shift to the inlet. The stress in the nozzle with a thickness of 3 mm first increases and then decreases, with a maximum stress of 139.43 MPa at t = 51.20 s. For nozzles of different thicknesses, the positions of the maximum stresses all appear at the outlet and the moments concentrate in approximately 50 s. However, with the increase in thickness, the maximum stress of nozzle increases continuously, and the maximum increases by 93% compared with the minimum.

Article History
Received May 21, 2023
Revised July 22, 2023
Accepted August 7, 2023
Available online October 8, 2023

Keywords:
Serpentine nozzle
Thermal–solid interaction
Flow heat transfer
Structure response
Wall thickness
Circular-to-rectangular profile

1. INTRODUCTION

With the rapid development of detection technology, future aircraft must have ultrahigh combat survivability. A low observable signature is one of the key technologies that future aircraft must possess, also known as stealth performance (Arif et al., 2018). Infrared radiation signature is a detectable signal of an aircraft, mainly from the exhaust system (Buchlin, 2010; Thillaikumar et al., 2020; Wang et al., 2020; Song et al., 2021). Because a serpentine nozzle can significantly reduce the infrared radiation emitted by engine exhaust, it has received widespread attention from various countries. Its research results have been used in advanced aircraft, such as the stealthy B-2 bombers. Several studies have investigated the use of serpentine nozzles.

An et al. (2016) investigated the infrared radiation characteristics of a serpentine nozzle wake flame for different outlet aspect ratios and compared the results with those of an axisymmetric nozzle. Harloff et al. (1992) used the PARC3D code to calculate compressible turbulent flow in a three-dimensional diffusionless S-shaped pipe to provide a reference for the study of secondary flow. Miau et al. (1988) investigated a circular-turned-square serpentine nozzle with three different lengths based on the Reynolds number at the inlet boundary layer thickness and the core zone velocity of the inlet. Reichert & Hingst (1991) conducted an experimental study on the effects of swirling flow on the flow characteristics of a serpentine nozzle. This result was used for subsequent comparisons with the results predicted by numerical simulation. Sun (2018) investigated the effects of the key design parameters of a serpentine nozzle on the flow characteristics. Cheng (2018) studied the effects of different shading rates on the infrared characteristics of a serpentine nozzle. The results of the numerical study were compared with the calculated infrared radiation characteristics of a circular nozzle. The results showed that the serpentine nozzle could reduce infrared radiation by 28.9%. Published literature has mainly focused on the infrared radiation and flow characteristics of serpentine nozzles. Serpentine nozzles are subjected to aerodynamic,

Nomenclature

A_1/A_{in}	the first bend exit area ratio	W_1/D	the first bend exit width ratio
L_2/L_1	axial length ratio of first S passage to second S passage	$\Delta Y_1/L_1$	ratio of offset distance to axial length of first S passage
L/D	ratio of axial length to inlet diameter	$\Delta Y_2/L_2$	ratio of offset distance to axial length of second S passage
W_e/H_e	aspect ratios of outlet		

thermal, acoustic, and structural loads transmitted by the supporting substructures during flight at hypersonic speeds (Crowe et al., 2015; Luo & Zheng, 2016). These multiple physical field loads make the structural response of the serpentine nozzle more complex than that of conventional nozzles, owing to its S-shaped passage with a large curvature and circular-to-rectangular profile. Therefore, it is necessary to conduct research on the structure of serpentine nozzles. However, the structural response of serpentine nozzles has been documented in only a few published studies.

In a serpentine nozzle afterdeck, the structure is prone to material buckling owing to thermal expansion. Increasing the wall thickness to suppress expansion may create counterforces due to the presence of supports (Haney & Grandhi, 2009). Researchers have modelled the structure of a nozzle afterdeck with a unit-width plate and explored the structural response of the plate under thermal loads from both clamping boundary and spring boundary conditions. Deaton & Grandhi, (2010) developed a coupled design framework for a serpentine nozzle and its surrounding support structure using the commercial finite element software NASTRAN. The thermal structural analysis of the serpentine nozzle was performed at a given temperature of the inner wall surface and the surrounding ambient temperature. The effects of the pressure and thermal loads on the structural response were then investigated. The results showed that the thermal stress was mainly contributed by the thermal load. Deaton & Grandhi (2011) also developed a transient thermal structural optimisation framework based on the MD NASTRAN and GENESIS commercial software. The serpentine nozzle structure was modelled with a triple truss and a composite plate, and the thermal structural response was explored under a given boundary condition. In addition, a thin-shell model was developed to investigate the effects of different boundary stiffness conditions on the structural responses of a serpentine nozzle (Deaton & Grandhi 2012). A simplified beam model was developed to investigate the effects of two different boundary conditions (clamped and simply supported) on the stress responses of a structural system under different structural parameters (curvature and thickness) and temperatures (Deaton & Beran 2016). Serpentine nozzles operate in a complex environment with high temperature and pressure, and nonlinear factors cannot be ignored in the structural design process. Deaton & Martin (2015) found that geometric nonlinearity is essential in the stress-strengthening behaviour by comparing the thermal structural responses in both linear and nonlinear cases. Urbanczyk et al. (2017) developed a multiphysics field analysis and optimisation framework based on a serpentine nozzle. This optimisation framework uses a one-way sequential coupling approach to optimise the design of a UAV exhaust system. The results indicate that the nozzle thickness was approximately 3.2 mm. However, the thicknesses at the nozzle connection with the support structure, nozzle throat, and nozzle outlet were as high as 20 mm. In the same year, a US-based intelligence company (Nigam et al., 2017) adopted this framework to perform a one-way flow-thermal-solid coupling analysis of a single internal culvert nozzle. The stress in the exhaust system is primarily attributed to the thermal load rather than to the aerodynamic load. Sun et al. (2022) conducted a study on the flow-solid two-way coupling for a serpentine nozzle and obtained the structural deformation characteristics of the nozzle and its internal/external flow characteristics. Based on the flow-solid two-way coupling method, Li et al. (2023) explored the effects of the outlet aspect ratio on the flow characteristics and aerodynamic performance of a serpentine nozzle.

In summary, in terms of the serpentine nozzle structure, previous research has mainly consisted of a structural analysis simplified to a two-dimensional model or given boundary conditions. However, the obtained calculation results are difficult to apply to three-dimensional structures. In addition, for the three-dimensional structure of a serpentine nozzle, researchers have considered the effect of fluid-structure coupling between the flow-field pressure and structural deformation. However, the serpentine nozzle is subjected to high-temperature gas expansion and internal impacts. This behaviour leads to an extremely complex temperature and thermal stress response, whereas the effect of the structural temperature boundary on the flow-field heat transfer is not negligible. Therefore, for a three-dimensional serpentine nozzle, the structural temperature and thermal stress fields must be calculated and analysed. Simultaneously, to consider the influence of structural temperature on flow-field heat transfer, it is necessary to investigate the mutual coupling of the flow field and its structure. In addition, the wall thickness is an important structural factor for the design of serpentine nozzles. However, the thickness has not been investigated for the temperature and thermal stress response laws under the mutual coupling effect of the flow field and structure. Therefore, this study aims to perform a thermal-solid coupling study between the flow field and structure of the serpentine nozzle in three dimensions. The outline of this paper is as follows. First, the thermal-solid coupling strategies utilised in this study are introduced. The accuracy of the thermal-solid coupling method was verified using NASA's Ma 6.47 aerodynamic heating experiment on the leading edge of a circular pipe, and the results are presented. Second, the flow-field and structural computational domain models of the serpentine nozzle are introduced. A numerical study of the thermal-solid

coupling of the serpentine nozzle was conducted, and the heat transfer mechanism from the internal flow field of the nozzle to the structure, the structural temperature, and the stress response are elucidated. Finally, the influence of the wall thickness of the serpentine nozzle on the thermal-solid coupling response was investigated, as described in Section 4.

2. NUMERICAL ALGORITHM

Cao et al. (2009) compared various flow and structural field coupling calculation methods. These researchers revealed that the mesh-based parallel code coupling interface (MpCCI) is more accurate as a multiphysics field-coupling calculation platform for achieving coupling calculations. MpCCI controls the coupling flow and enables data exchange between different physical fields. The software can identify and match the coupled neighbourhood meshes of different physical fields independently. The structural analysis software ABAQUS was used to run the INP text file through the programs of the MpCCI, and the UDF function files were created by the MpCCI to operate the flow field calculation software FLUENT which ran simultaneously. Therefore, a thermal-solid coupling numerical simulation was conducted. In this study, the physical parameters exchanged between the flow and structure fields were the wall temperature and heat flux.

2.1 Fluid Dynamic Solver

The density-based flow solver FLUENT uses the finite volume method to solve unsteady Reynolds-averaged Navier–Stokes equations. In addition, the AUSM+ spatial format and SST *k-w* dual equation model were adopted to accurately capture the physical details of the high-speed compressible flow inside the serpentine nozzle, particularly the near-wall aerodynamic heating flow field simulation with high accuracy. The AUSM+ spatial format exhibits excellent performance such as strong intermittent resolution, good positive fixation retention, and no "carbuncle" phenomenon (Liou, 2001). Owing to the choice of the SST *k-w* dual equation for the turbulence model, the mesh was divided such that the y+ values of the first-layer grid were required to satisfy this turbulence model (Guo et al., 2016). To calculate the heat flux q occurring in the first-layer grid near the wall of the flow field, the following equation was used:

$$q = -\lambda \nabla T, \tag{1}$$

where ∇T is the temperature gradient, and the negative sign indicates that the direction of heat transfer is opposite to the direction of temperature rise. λ is the thermal conductivity.

2.2 Structure Dynamic Solver

Based on the finite element method, ABAQUS was used to analyse the structural response. The control equations to be solved mainly included heat conduction and physical equations considering thermal expansion. Due to the transient heat transfer process, the heat conduction equation can be expressed as follows:

$$[C]\{\dot{T}\}+[K]\{T\}=\{Q\}, \tag{2}$$

where $[C]$ is the specific-heat matrix. $\{T\}$ is the node temperature vector, $\{\dot{T}\}$ is the temperature derivative over time, and $[K]$ is the conduction matrix. $\{Q\}$ is the node heat flux rate vector. In addition, $[K]$ represents the temperature dependence of the thermal properties of the material.

The temperature difference(ΔT) inside the object causes thermal expansion. The expansion amount is $\alpha_T \Delta T$, and α_T is the coefficient of thermal expansion. The physical equation is then given by

$$\begin{cases} \varepsilon_{xx} = \dfrac{1}{E}\left[\sigma_{xx} - \gamma(\sigma_{yy}+\sigma_{zz})\right] + \alpha_T \Delta T \\ \varepsilon_{yy} = \dfrac{1}{E}\left[\sigma_{yy} - \gamma(\sigma_{xx}+\sigma_{zz})\right] + \alpha_T \Delta T \\ \varepsilon_{zz} = \dfrac{1}{E}\left[\sigma_{zz} - \gamma(\sigma_{yy}+\sigma_{xx})\right] + \alpha_T \Delta T \\ \gamma_{xy} = \dfrac{1}{G}\tau_{xy} \\ \gamma_{yz} = \dfrac{1}{G}\tau_{yz} \\ \gamma_{zx} = \dfrac{1}{G}\tau_{zx} \end{cases} \tag{3}$$

where E is the elastic modulus and γ denotes Poisson's ratio.

2.3 Thermal–Solid Coupling Strategies

The solution for the thermal–solid interaction was implemented using MPCCI. As a multiphysics coupling platform, this software enables accurate control of the coupling process and iterative exchange of data between FLUENT and ABAQUS. The solvers solved control equations for different physical fields.

In the coupling calculation, the interface between the flow field and structure field must satisfy the conditions of temperature continuity and heat equilibrium, as follows:

$$T_f = T_s, \tag{4}$$

$$k_s \nabla T_s \cdot \vec{n}_s = -k_f \nabla T_f \cdot \vec{n}_f, \tag{5}$$

where T_f and T_s represent the temperatures of the flow and structure fields nodes on the coupling surface, respectively. k_f and k_s represent the thermal conductivity of the fluid domain and the structural domain, respectively.$\vec{n}_f$ and $\vec{n}_s$ represent the flow field side wall normal vector and the structure side wall normal vector, respectively. Their relationship can be obtained as follows:

$$\vec{n}_f = -\vec{n}_s. \tag{6}$$

Before the coupling solution was applied, an initial steady flow field was obtained at the given thermal boundary of the coupling surface temperature. At the initial moment of the coupling calculation, in the data transfer platform MpCCI, the initial state of FLUENT is "send", i.e., it is ready to transfer the calculated heat flux data to ABAQUS, and the initial state of ABAQUS is "receive", which enables the receipt of the heat flux data and uses them as an external thermal load for structural calculations. Subsequently, the structural solver begins the

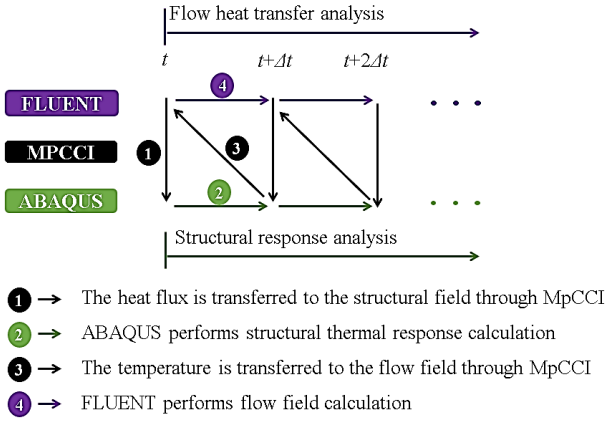

Fig. 1 Data transfer diagram

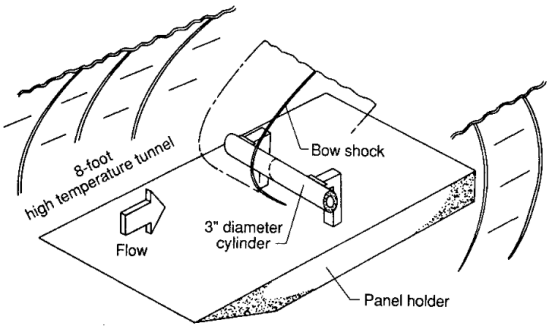

Fig. 2 Experimental configuration (Wieting, 1987)

thermal analysis; in other words, the coupling calculation begins. The MpCCI transfers the coupling surface temperature from the thermal analysis results to the coupling surface of the flow field as a new temperature boundary for the flow field calculation in preparation for the next coupling iteration. The data transfer process is illustrated in Fig. 1.

Figure 1 shows the following. (1) The MpCCI extracts the calculation solution of the coupling surface of the flow field at time t from FLUENT and maps it to the corresponding structural grid. (2) ABAQUS obtains the flow field data (heat flux) transferred from the MpCCI at time t. The data become boundary conditions for thermal analysis at period (t, $t+\Delta t$) to obtain the structural response, including stress and temperature distribution at time $t+\Delta t$. (3) After the structural response calculation is completed, MpCCI extracts the structural temperature of the coupling surface and maps it to the corresponding flow field grid. (4)FLUENT obtains the new temperature boundary value through MpCCI and calculates the flow field in the period (t, $t+\Delta t$). Finally, FLUENT obtains the heat flux of the flow field at time $t+\Delta t$ and prepares for the next iteration. Giles (1997) indicated that the temperature boundary condition is obtained from the structure field, and the heat flux boundary condition is obtained from the flow field, which can improve the stability of the numerical calculation of the coupling.

2.4 Verification for Coupling Algorithm

Wieting (1987) completed a leading-edge heating

Table 1 Freestream conditions (Wieting, 1987)

Ma_∞	T^*/K	P^*/Pa	Re_∞
6.47	241.5	648.1	1.31×10^6

Table 2 Material thermal properties

ρ (kg/m^3)	C_p (J/Kg·K)	K (W/m·K)
8030	502.48	16.27

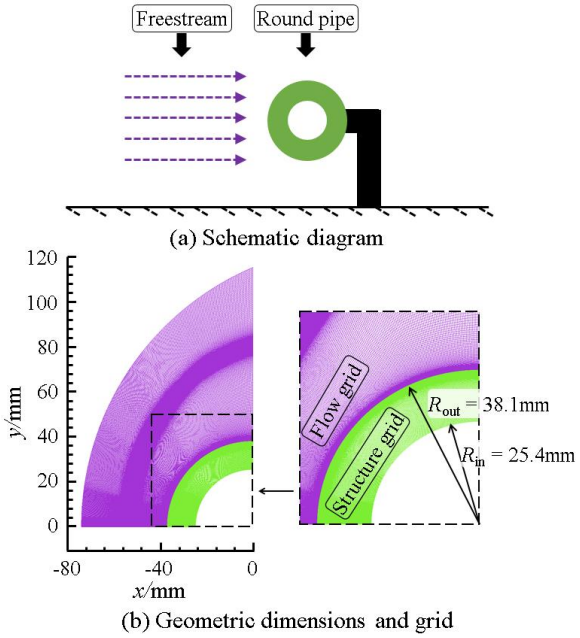

Fig. 3 Meshes of flow field and structure field

experiment of an infinitely long stainless-steel round pipe under hypersonic conditions and shock wave interference in an 8-ft high-temperature wind tunnel at the NASA Langley Research Center in 1987. The study focused on the variations in the peak heat flux at the wall of a circular pipe in the presence of an oblique shockwave-disembodied shockwave. The experimental data served as a reference to verify the accuracy of the numerical method used in the current study. Figure 2 shows a diagram of the experimental configuration. The freestream conditions are listed in Table 1, and the thermal properties of the structural materials are listed in Table 2. The incoming gas had $Pr = 0.71$, the inner diameter of the stainless-steel pipe was 25.4 mm, and the outer diameter was 38.1 mm.

Figure 2 was simplified as Fig. 3(a). It can be observed that the symmetry of the computational domains of the flow and structural fields is considered, and part of the flow and structural computational models were divided into meshes, as shown in Fig. 3(b) (Guo et al., 2016; Dechaumphai et al., 1988, 1989). Combined with previous studies (Guo et al., 2016; Dechaumphai et al., 1988, 1989), the height of the first grid of coupling surface for flow field was set to 3×10^{-6} m, and the boundary-layer mesh was graduated normal to the cylinder surface by an incremental factor of 1.1. The SST k-w two-equation model was selected to capture the physical details of the viscous substratum and logarithmic layers.

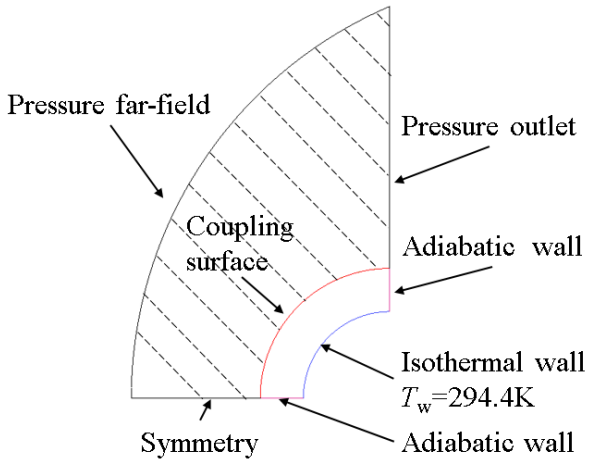

Fig. 4 Boundary conditions of the flow field and structure field

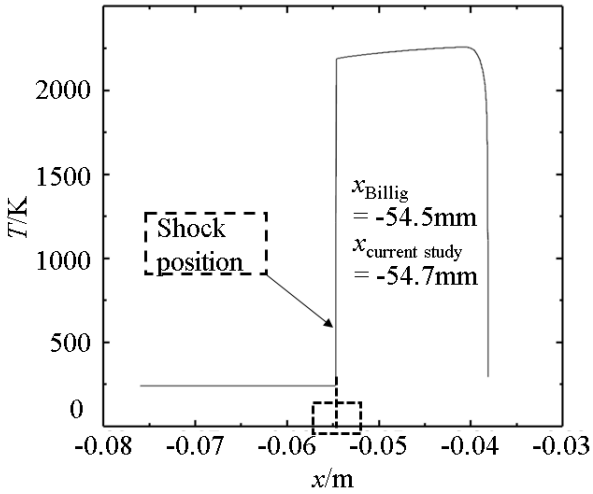

Fig. 5 Temperature distribution along the flow symmetry line

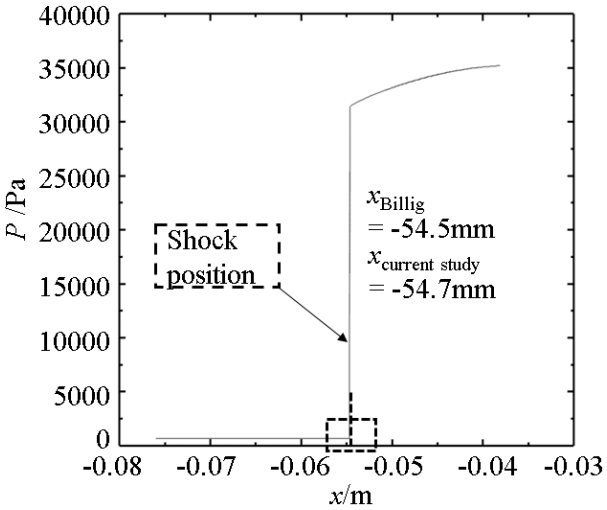

Fig. 6 Pressure distribution along the flow symmetry line

The boundary conditions of the flow and structural fields are shown in Fig. 4. The initial temperature of the structure was identical to the ambient temperature of 294.4 K Prior to coupling calculations, the flow field must reach a steady state. Figures 5 and 6 show the temperature and

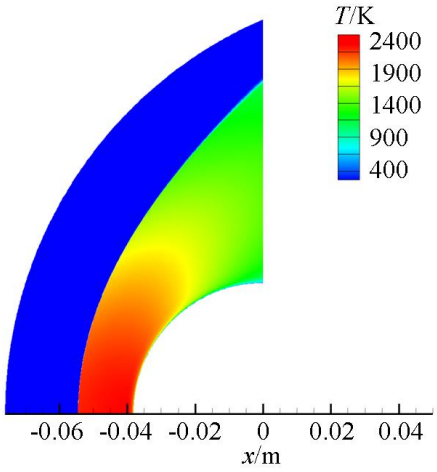

Fig. 7 Temperature distribution

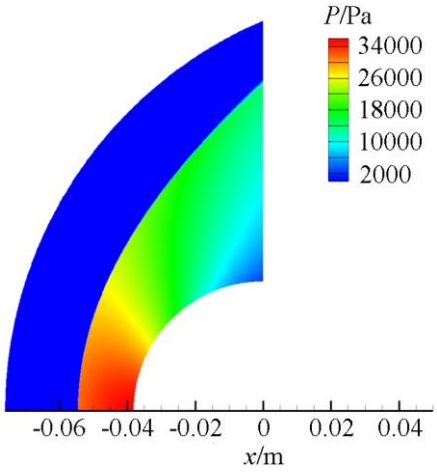

Fig. 8 Pressure distribution

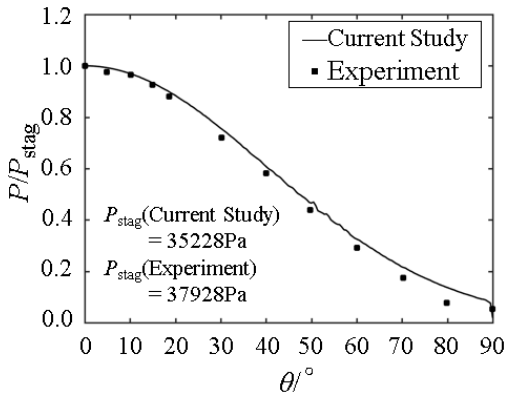

Fig. 9 Comparisons between predicted and experimental pressure distribution

pressure distributions along the flow symmetry line, respectively. In this section, the shock wave occurs at x =−54.7 mm, and it is within 1% of the theoretical formula calculation result x = −54.5 mm, which shows a high degree of agreement (Billig, 1967). Figures 7 and 8 show the flow field temperature and pressure distributions, respectively.

Figure 9 shows the pressure distribution on the wall of the round pipe. The predicted pressure distribution normalised to the stagnation point values agrees well with the experimental results. The maximum deviation between

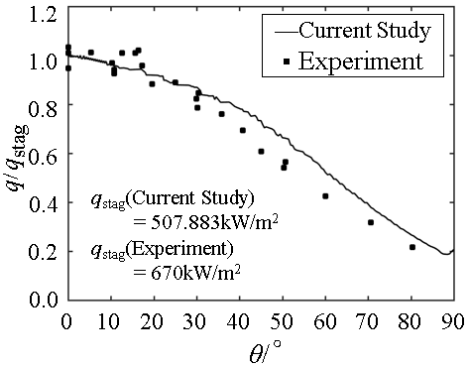

Fig. 10 Comparisons between predicted and experimental heat flux distribution

Table 3 Comparison of results of peers

References	P_{stag}/Pa	q_{stag}/(kW/m²)
(Wieting, 1987)	37928	670.035
(Guo, et al. 2016)	35242	546.400
Current study	35228	507.883
(Zope, et al. 2020)	35230	504.806
(Dechaumphai, 1988)	-	482.652
(Kamali, et al. 2020)	35147	469.660

the simulation results and the experimental stagnation point pressure was 7.12%. This deviation is partly caused by the inconsistencies in the physical parameters of the gas. This is because the flow medium used in the numerical simulation was an ideal gas, whereas in the experiment, the flow medium was the combustion product of methane and air.

Figure 10 illustrates the heat flux distribution on the coupled wall of the round pipe. The predicted heat fluxes normalised to their respective stagnation point values agree well with the experimental results. This study compared the relevant calculations of international peer researchers to evaluate the precision and accuracy, as shown in Table 3.

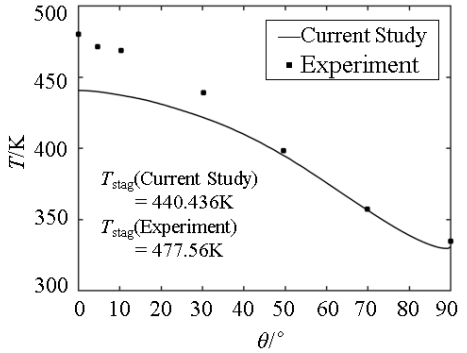

Fig. 11 Comparisons between predicted and experimental temperature distribution

Table 4 Comparison of results of peers

References	T_{stag}/K
(Zope, et al. 2020)	464
Current Study	**441**
(Guo, et al. 2016)	438

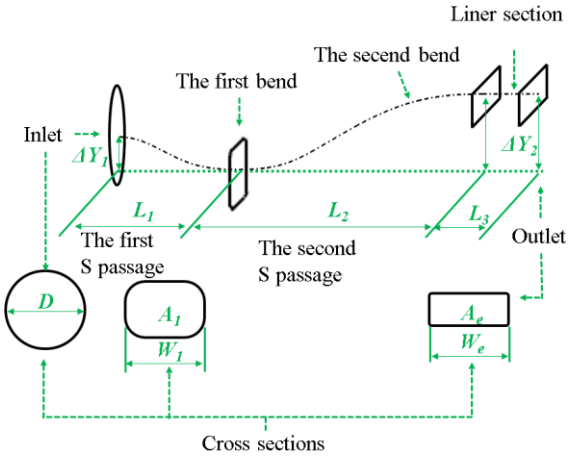

Fig. 12 Design parameters of the serpentine nozzle

Figure 11 shows the temperature distribution along the outer surface (coupling surface) of the pipe at the final moment. Because the predicted stagnation-point heat flux in the initial steady-state flow field calculation was lower than the experimental value, the maximum difference between the results and experimental values at t = 5 s was within 7.7%. This study compared the relevant solutions of the studies conducted by international peer researchers, as listed in Table 4.

According to the comparisons in the two tables above, the accuracy and precision of the results of this study are comparable to those at the international level. This section describes the computational fluid dynamics (CFD)/computational solid dynamics (CSD) methods based on the MpCCI used to verify the thermal-solid coupling calculation under supersonic/hypersonic conditions. Hence, the accuracy and precision of the adopted thermal-solid coupling strategy can be accepted and adopted for subsequent analyses.

3. RESEARCH ON THERMAL-SOLID COUPLING OF SERPENTINE NOZZLE

3.1 Description of Geometry Model

The design parameters of the serpentine nozzle are presented in Fig. 12. The two S passages consist of a series of cross-sections perpendicular to the centreline, which are formed by splicing two Lee curves (Lee et al., 1985; Sun et al., 2015), as shown in the L_1 and L_2 sections in Fig. 12. The cross-section gradually transforms from a circular inlet to a rectangular outlet, as shown in the L_3 section in Fig. 12. The purpose of the liner section at the outlet is to provide a uniform outlet airflow.

Figure 13 shows the geometric model of the serpentine nozzle, including the additional linear section of the inlet. The thickness of the reference model is 3 mm. The geometric parameters of the pneumatic surface of the serpentine nozzle (inner wall surface of the serpentine nozzle) include the ratio of axial length to inlet diameter L/D = 2.43, axial length ratio of the first S passage to the second S passage L_1/L_2 = 0.67, aspect ratio of outlet W_e/H_e = 4.00, first bend width ratio W_1/D = 1.11, first bend area ratio A_1/A_{in} = 0.60, and a shading rate of 0.25. The total length L of the nozzle is 186.50 mm.

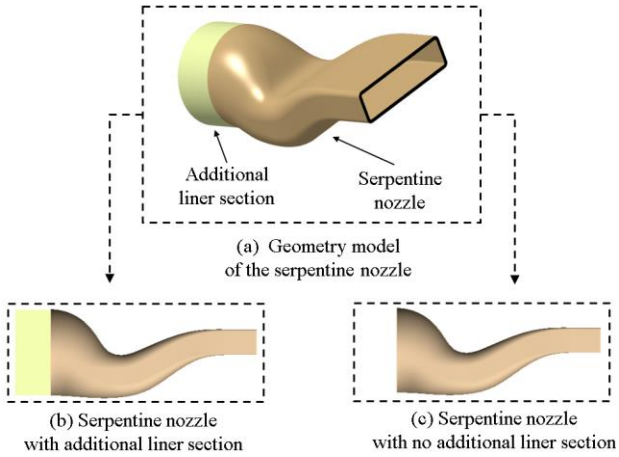

Fig. 13 Geometry model of the serpentine nozzle

In front of the nozzle inlet, a yellow linear section was added, as shown in Fig. 13(b). Fig. 13(c) shows the linear section before the addition of the inlet. Fig. 13(c) shows that if the liner section is not added before the nozzle inlet, when the airflow enters the nozzle, the airflow near the upper wall rotates immediately along the upper physical wall of the nozzle owing to the effect of the nozzle configuration. Numerous numerical simulation results show that if a liner section is not added, the simulation will not easily converge at the upper wall at the outlet, while adding a small liner section at the entrance can effectively solve the problem. Therefore, to maintain the structural field computational domain, the flow field domain includes a corresponding linear section.

3.2 Flow Field Calculation Model

Figures 13 and 14 depict the flow field model and computational mesh, respectively. Pressure inlet conditions were applied to the nozzle inlet with a total pressure of 155817.60 Pa and a total temperature of 1071.87 K. The far-field domain outlet was defined as the pressure outlet condition with a static pressure of 101325 Pa and a static temperature of 300 K. Other boundaries except for coupling wall surfaces between the flow field and the structure field were set to pressure far field condition, with $Ma_\infty = 0.05$ and static pressure 101325 Pa. The coupling wall surfaces were set to a constant temperature in the initial steady flow field prior to the coupling calculation.

The flow field solver FLUENT is based on density and uses the AUSM+ computational format with low numerical dissipation, high resolution of surge and contact intermittency, no entropy correction, and high computational efficiency. The SST k-ω dual-squared turbulence model adopted in this study can capture the details of heat transfer in the viscous bottom and logarithmic layers of the flow. In addition, spatial discretisation was performed in a second-order windward format. The flow medium was an ideal gas. The local grid encryption at locations with large structural curvatures is shown in the flow field domain grid in Fig. 15. In addition, the y+ values of the first-layer grid near the wall had a magnitude of 1.

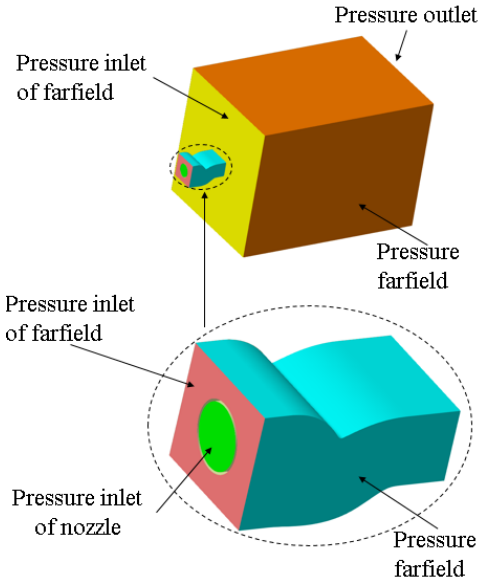

Fig. 14 Computational model of flow field

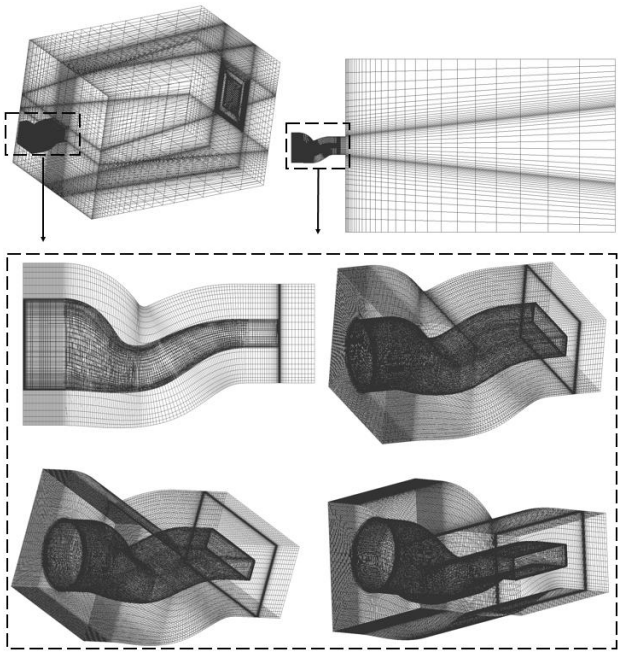

Fig. 15 Computational mesh of flow field

3.3 Structural Calculation Model

Figure 15 shows the finite element model of the serpentine nozzle with a structural grid distribution. The grid element type was the C3D8RT in ABAQUS. The rigid-body displacement affects the thermal stress of the serpentine nozzle. Therefore, geometric boundary conditions were applied to ensure the restraint of the rigid-body displacement such that the serpentine nozzle could expand freely, and the stress of the nozzle was completely generated by the thermal load. The displacement constraints were as follows: the displacements of Point 1 in the three directions (x y z) were zero, the displacements in the x and y directions were zero for Point 2, and the displacements of Point 3 in the x and z directions were zero. Figure 16 shows the positions of the three points.

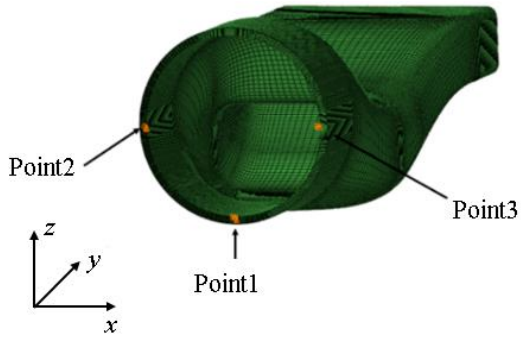

Fig. 16 Finite element model and positions of constraint points

Table 3 Material thermal properties

T/K	k/(W/(m·K))	E/GPa	γ
293.15	12.5	210	0.382
373.15	14.0	206	0.389
423.15	14.8	-	-
473.15	15.9	200	0.389
523.15	16.7	-	-
573.15	17.6	194	0.392
623.15	18.5	-	-
673.15	19.2	188	0.405
723.15	19.9	-	-
773.15	20.6	181	0.404
823.15	21.3	-	-
873.15	22.1	174	0.395
973.15	-	166	0.415

Inconel 706, a high-temperature alloy used in the serpentine nozzles of the Swedish Defence Research Agency (Smith & Dalenbring, 2006) was selected for this study. Its density (ρ) is 8100 kg/m^3, the thermal expansion coefficient (α_T) is 1.346×10^{-5}, and the specific heat capacity (C_p) is 445.456 J/(kg·K). In addition, the modulus of elasticity (E), Poisson's ratio (γ), and thermal conductivity (k) are temperature-dependent, as shown in Table 3.

3.4 Sensitivity Analysis

The grid is an important factor in aerothermal numerical simulations and has become the consensus of researchers (Pan, 2010). This is because, with respect to the aerodynamic thermal properties, in addition to the basic requirements for mesh quality inside the flow field, the requirements for the mesh near the wall are more stringent. The heat flux is generated at the wall between the fluid and solid. Therefore, the quality of the grid near the wall directly affects the accuracy and precision of the numerical simulation of the flow field.

The temperature distribution used to calculate the heat flux in the boundary layer near the wall is particularly critical. Therefore, the key to an aerothermal numerical simulation is obtaining an accurate flow-field temperature distribution. According to the temperature distribution in the boundary layer, there are three main types of thermal boundary conditions: adiabatic wall, constant cold wall, and constant hot wall, as shown in Fig. 17. When the wall temperature is lower than the airflow temperature, the wall

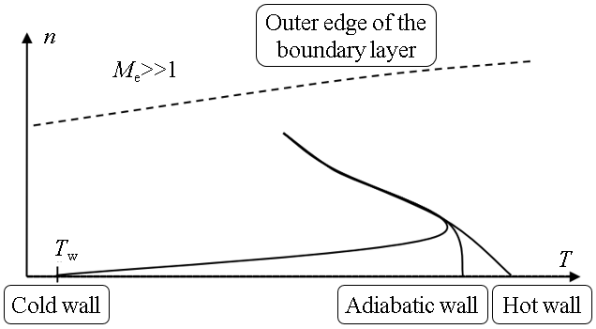

Fig. 17 Temperature distributions in boundary layer under different wall conditions (Pan, 2010)

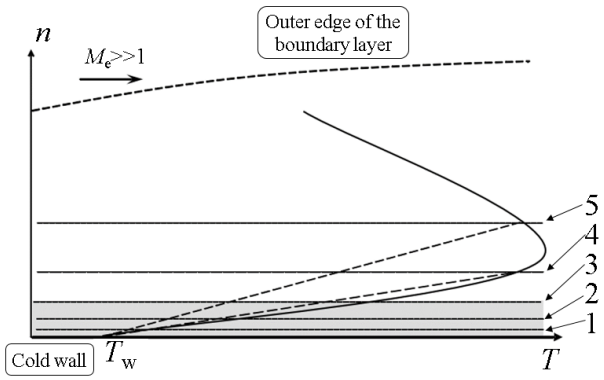

Fig. 18 Schematic of grid requirements in boundary layer (Pan, 2010)

is heated by the airflow. In this case, the wall is called a constant cold wall, and the opposite is true for the constant heat wall. The adiabatic wall is expressed as the airflow temperature being the same as the wall temperature, such that there is no heat exchange. In this study, an aerothermal simulation was conducted to determine the temperature distribution in a constant cold wall. The wall temperature is generally considerably lower than the adiabatic wall temperature according to the requirements of engineering design, as shown in Fig. 17.

According to the formula of heat flux ($q=\lambda(\partial T/\partial x)_w$), it is essential to arrange a sufficiently fine grid near the wall to accurately simulate the near-wall temperature distribution to build the near-wall heat flux distribution. By discretising the formula as $(T-T_w)/\Delta_w$, Δ_w represents the height of the first-layer grid. From a mathematical perspective, the result of the formula represents the slope of the temperature distribution curve. Figure 18 shows a schematic of the grid requirements for the boundary layer. The first grid height can be the height of any grid line, such as the first, second, third, fourth, and fifth grid lines, as shown in Fig. 18. Inside the linear layer of the temperature boundary layer, the slopes obtained by the first, second, and third grid lines are the same as those in Fig. 18. If the first layer of the mesh height continues to increase to the fourth and fifth layers, the slopes will significantly differ. Therefore, the grid height of the first layer is critical for the correct heat flux distribution.

Figures 19 and 20 illustrate the static pressure and heat flux distribution on the upper and the lower symmetrical surfaces of the inner wall of the serpentine

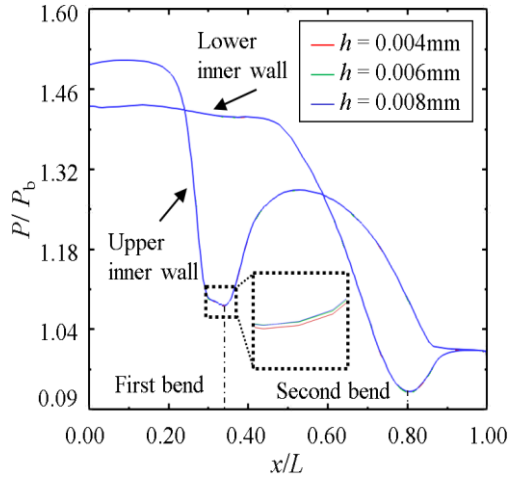

Fig. 19 Comparison of static pressure distributions on symmetrical surface of inner wall under different first layer grid heights

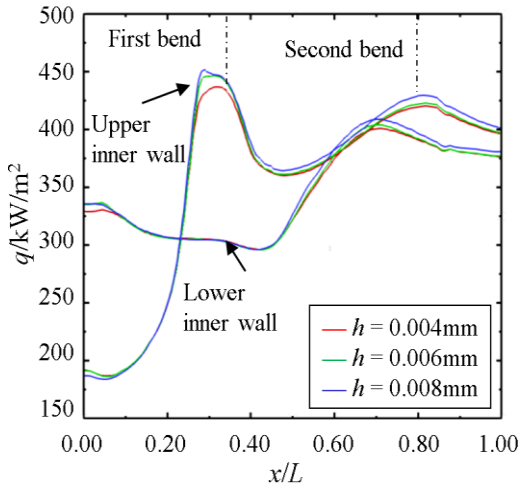

Fig. 20 Comparison of heat flux distributions on symmetrical surface of inner wall under different first layer grid heights

nozzle under different grid heights of the first layer (h represents the grid height of the first layer: $h = 4\times10^{-6}$ m, $h = 6\times10^{-6}$ m, and $h = 8\times10^{-6}$ m). According to the results for the three grid heights, the maximum errors of the pressure and heat flux were less than 0.1% and 0.8%, respectively, indicating that the results were grid-independent. Therefore, to ensure accuracy and reduce the time, the grid corresponding to the boundary layer height $h = 6\times10^{-6}$ m was selected to analyse and mesh the flow field of other serpentine exhaust configurations.

For the verification of the coupling time step independence, two sets of time steps were given as Δt = 0.08 s and Δt = 0.05 s, respectively. The total time was set to 300s to ensure that the nozzle temperature distribution was close to steady state at the final moment. Figure 21 shows the time evolution of the temperature at the feature points under different time steps. The maximum relative error between the two was less than 3.7%, which indicates that Δt = 0.08 s has met the calculation requirement. Therefore, Δt = 0.08 s was selected as the coupling time step and used in the thermal-solid coupling analysis of other serpentine nozzle configurations.

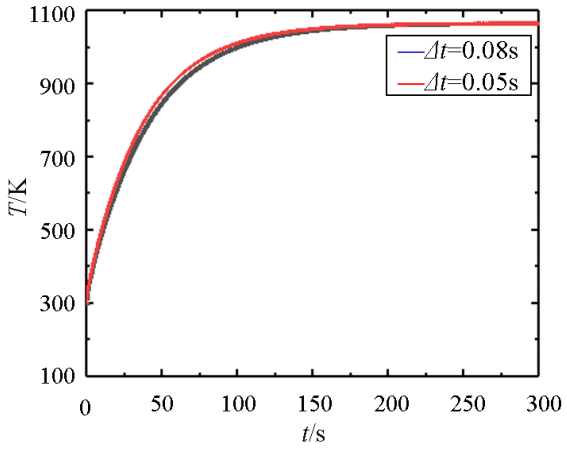

Fig. 21 Time evolutions of temperature at feature points under different time steps

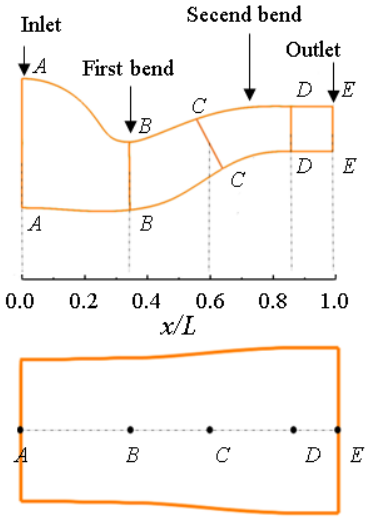

Fig. 22 Axial locations of the cross-sections inside the serpentine nozzle

3.5 Flow Heat Transfer Analysis of Steady-State Flow Field

Before the thermal-solid coupling starts, it is necessary to obtain a solution for the steady-state flow field of the serpentine nozzle to prepare for the coupling calculations. The structural features of the serpentine nozzle include curved surfaces and S-shaped channels, different transitions along the cross-section, and a binary nozzle geometry configuration. These features make the flow field inside the nozzle complex, such as the local acceleration and uneven distribution of aerodynamic parameters. Owing to these flow characteristics, the internal heat transfer mechanism of the nozzle becomes complicated, and a detailed flow heat transfer analysis is required to better understand the structural response of the subsequent serpentine nozzle.

The flow heat transfer of the serpentine nozzle is closely related to the geometric configuration. To simplify the analysis, the cross-sections of the nozzle were given along the axial variation pattern, as shown in Fig. 22. In the second S passage, cross section C–C is at x = 0.6, whereas cross section D–D is located at the beginning of the straight section of the outlet.

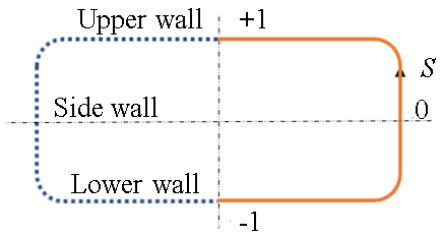

Fig. 23 Dimensionless coordinate system of the peripheral wall

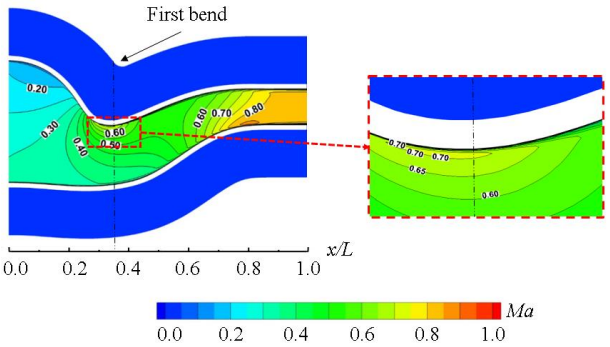

Fig. 24 Mach number distribution on the symmetry surface of the serpentine nozzle

In addition, the wall circumferential dimensionless coordinate was established and defined, as shown in Fig. 23. The midpoint of the lateral wall was defined as the coordinate origin S = 0, whereas the midpoints of the upper and lower walls were S = +1 and S = -1, respectively.

The airflow was deflected as it passed through the serpentine nozzle. The difference in the curvature of the structure at the turn of the flow path led to different streamline curvatures. This phenomenon caused different degrees of contraction of the airflow tube and led to differences in the acceleration intensity. The stronger the acceleration, the larger the velocity gradient near the wall and the thinner the velocity boundary layer. Therefore, the thinner the thermal boundary layer, the stronger the heat transfer.

Figure 24 shows the distribution of the Mach number on the symmetry surface of the serpentine nozzle (excluding the linear section of the inlet and far field). Inside the serpentine nozzle, the airflow gradually accelerated, and there were local acceleration zones in the first and second bends. The Mach number distribution is uneven. The static pressure distribution on the symmetrical surface is also closely related to the velocity.

When the airflow entered the nozzle, owing to the shape of the structure, the streamline was bent, and the airflow was subjected to a centripetal force at the turn. The centripetal force was provided by the force due to the pressure-difference perpendicular to the streamline. The centripetal force was directed towards the centre of the structural curvature. This pressure difference was caused by the variations in acceleration of the airflow at the turn. Considering the first bend as an example, the curvature of the upper wall of the nozzle was larger than that of the lower wall, and the variation in acceleration of the airflow was stronger than that of the lower wall. Hence, this

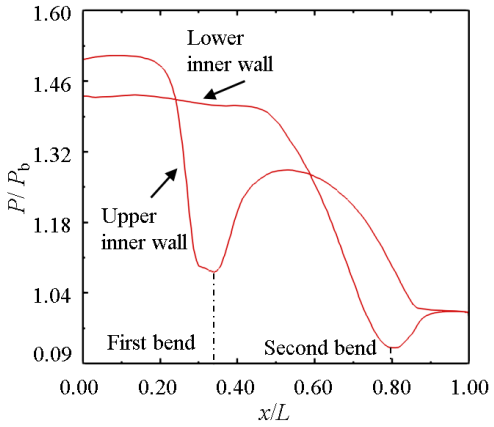

Fig. 25 Pressure distribution on the symmetry surface of the inner wall

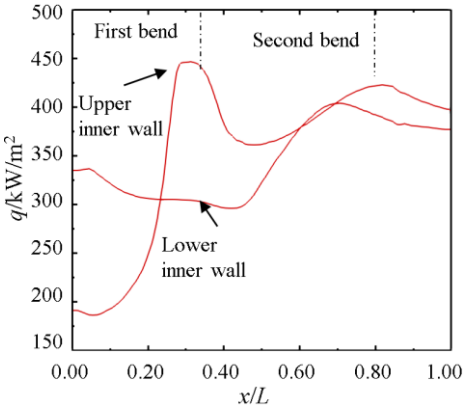

Fig. 26 Heat flux distribution on the symmetry surface of the inner wall

behaviour formed a pressure gradient towards the centre of curvature of the upper wall. The greater the curvature of the serpentine nozzle, the stronger the acceleration of the airflow, and the easier it was to form a local acceleration zone.

The static pressure and heat flux distributions on the upper and lower symmetric surfaces of the inner wall of the serpentine nozzle are shown in Figs. 25 and 26, respectively. In the first S passage, the curvature of the upper wall was greater than that of the lower wall, and the airflow near the upper wall was deflected downward. The pressure on the upper wall was greater than that on the lower wall to maintain the deflection movement of the airflow, as shown in Fig. 25. As illustrated in Fig. 26, because the curvature of the lower wall varied smoothly, the thermal boundary layer on the lower wall continued to thicken after the nozzle inlet, causing the heat transfer to weaken and the heat flux to consistently decrease. The airflow near the upper wall continuously accelerated, resulting in an increased heat exchange and a sharp increase in heat flux.

The closer to the upper wall of the first bend, the higher was the degree of contraction of the airflow tube and the stronger was the acceleration effect, which eventually led to the formation of a local acceleration zone on the upper wall of the first bend. The velocity reached a local maximum, whereas the static pressure decreased rapidly to a local minimum at the corresponding location.

In the right half of Fig. 24, the velocity first maintained a certain Mach number and then decreased. The thermal boundary layer thickened, and heat transfer weakened. Therefore, the heat flux at the upper wall remained locally unchanged at the first bend and then decreased, as shown in Fig. 26.

The curvature of the lower wall of the first S passage changed smoothly. Consequently, the velocity increased gradually, and the thermal boundary layer continued to increase along the path. This weakened the heat transfer and reduced the heat flux, as shown in Fig. 26.

After the first bend, the airflow tube near the upper wall expanded; thus, the airflow velocity decreased and the static pressure on the upper wall increased sharply. This led to a large adverse pressure gradient along the flow direction on the upper wall. Consequently, the thermal boundary layer became thicker, and the heat flux decreased in this region, as shown in Fig. 26.

In the second S passage, the airflow tube near the lower wall began to shrink quickly, the airflow began to accelerate, and the static pressure on the lower wall decreased. In the second bend, the airflow tube shrank, forming a local acceleration zone. After the second bend, the wall curvature decreased, the inner airflow tube expanded, the velocity decreased, and the static pressure on the lower wall increased.

Closer to the upper wall at the second bend, the airflow tube shrank, the speed increased, and the static pressure decreased gradually. After entering the straight section of the nozzle outlet, the static pressure on the upper and lower walls was consistent owing to the given nozzle drop pressure ratio and inlet and outlet areas.

The velocity at the lower wall increased continuously after the first bend until after the second bend, the flow tube expanded, and the speed decreased. Simultaneously, the heat transfer first increased after the first bend and then decreased. After entering the straight section of the outlet, the velocity no longer increased and the thickness of the thermal boundary layer continued to increase, as shown at the lower wall in Fig. 26.

After the first bend of the upper wall, the thermal boundary layer thickened, weakening the heat transfer and reducing the heat flux. Before the second bend of the upper wall, the airflow tube shrank, the airflow accelerated, the heat exchange was enhanced, and the heat flux increased. After entering the straight section, the airflow velocity ceased to increase. The thickening of the boundary layer weakened the heat transfer, and the heat flux gradually decreased. As shown in Fig. 26, inside the second S passage, the maximum heat flux on the upper wall occurred later than the maximum heat flux on the lower wall because the acceleration area of the upper wall was larger.

Because of the complexity of the internal field, local coordinate systems in the directions of airflow (l), normal (n), and transverse (m) were established at each cross section for convenience of analysis. Figure 27 shows the relationship between the local and global coordinate systems. Because the m direction is the same as the z

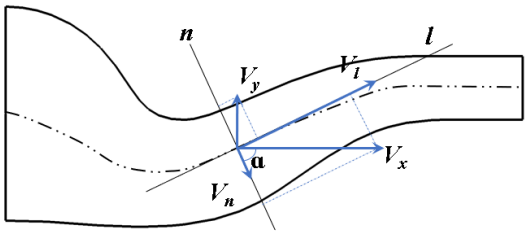

Fig. 27 Schematic diagram of velocity relationship (Sun, 2018)

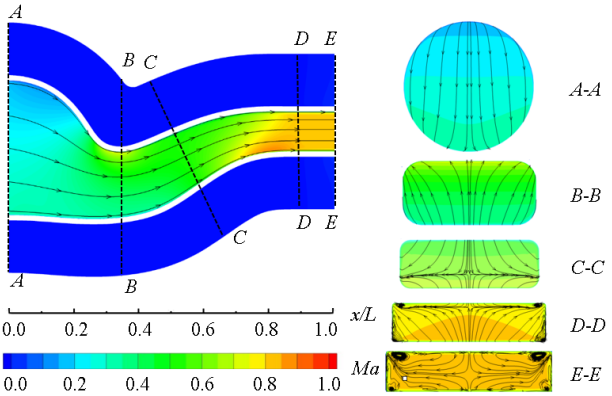

Fig. 28 Mach distribution and streamline distributions of symmetrical surface and cross-sections of the serpentine nozzle

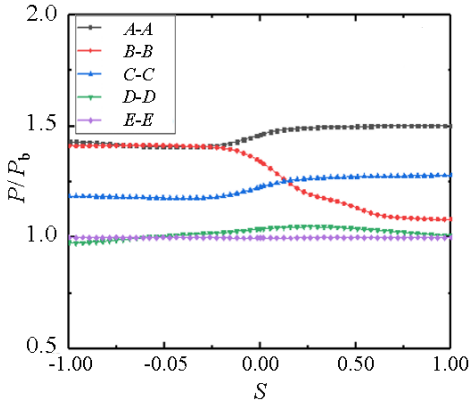

Fig. 29 Static pressure distributions on peripheral wall

direction and is perpendicular to the paper, it is omitted and not shown in Fig. 27. The velocities in the local (V_l, V_n, V_m) and global coordinate systems (V_x, V_y, V_z) satisfy the following relationship (Sun, 2018):

$$\begin{cases} V_l = V_x \sin\alpha + V_y \cos\alpha, \\ V_n = V_y \sin\alpha - V_x \cos\alpha, \\ V_m = V_z, \end{cases} \tag{7}$$

where α is the angle between the flow section and x-axis.

Figure 28 shows the Mach and streamline distributions of the symmetric surfaces of the serpentine nozzle and the cross-sections along the path. To analyse the corresponding formation mechanism, the static pressure distribution on the peripheral wall along the flow cross-sections is presented in Fig. 29.

In the symmetry plane, $V_m = V_z = 0$. In cross-section *A–A*, owing to the downstream channel configuration, $V_n = V_y < 0$. The streamlines in this cross-section were downward, as shown in Fig. 28.

In cross-section *B–B*, because the second S passage bent upward and the airflow moved upward, $V_n = V_y > 0$, leading to an upward flow. The passage after the first bend expanded laterally, as shown in Fig. 28. From the static pressure distribution on the peripheral wall shown in Fig. 29, the pressure on the lower wall is greater than that on the upper wall; therefore, the streamlines were oriented upward.

In cross-section *C–C*, the direction of the streamlines in the upper part was downward, whereas the direction of the streamlines in the lower part was upward. Both curves were curved towards the sidewalls. In the second S passage of the nozzle, the nozzle bent upward, and the airflow moved upward; therefore, $V_y > 0$ and $V_x > 0$. α was an acute angle. It can be seen from Eq. (4) that V_n can be positive or negative. When $V_n < 0$, the streamline direction was downward, whereas when $V_n > 0$, it was upward. The channel also expanded laterally and thus streamlines towards the sidewall. When $V_n = 0$ and $V_m \neq 0$, it represented the convergence of the downward and upward streamlines. In addition, as the curvature of the channel decreased from cross-section *B–B* to *C–C*, the centre of curvature also changed from the upper side to the lower side. Fig. 29 shows that from cross-sections *B–B* to *C–C*, the pressure difference between the upper and lower walls continued to decrease. Consequently, the direction of the pressure difference from cross-section *B–B* to cross-section *C–C* changed, as shown in Fig. 29.

The secondary flow of the vortex structure appeared in cross sections *D–D*. In the right part of the cross-section, under the action of the pressure difference between the side and upper walls, the flow near the wall moved upward along the wall, and the main flow moved to the lower right, thus forming a counterclockwise rotating vortex. Under the pressure difference between the side and lower walls, the flow near the wall moved downward along the side wall, and the main flow moved upward to the right, thus forming a clockwise vortex. In cross-sections *E–E*, a vortex still exists.

For the vortex in cross-sections *D–D* and *E–E*, the rotation velocity was inconsistent with the direction of the velocity of the mainstream and was perpendicular to the direction of the mainstream velocity. Therefore, it was difficult for the heat of the mainstream to be transferred to the wall through the vortex, which inhibited the heat transfer to the wall.

Figure 30 shows the heat flux distribution of the serpentine nozzle. Except in the local acceleration area, the heat flux increased from the inlet to the outlet. Owing to local acceleration, the upper wall at the first bend and lower wall at the second bend produced local extreme heat flux values. In addition, after the first bend, the nozzle geometry expansion led to a lateral airflow. The closer to the lower wall at the second bend, the larger the curvature of the wall and the stronger the acceleration effect. Hence, the closer they are to both sides of the nozzle, the greater

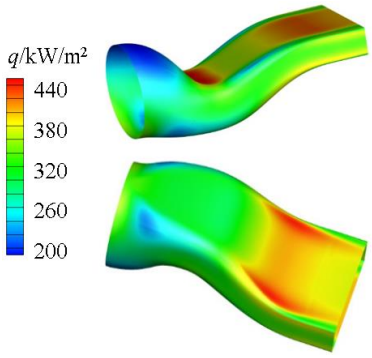

Fig. 30 Heat flux distribution on the inner wall of the serpentine nozzle

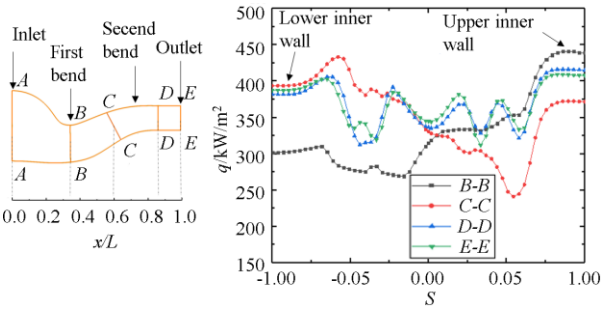

Fig. 31 Heat flux distributions on the peripheral walls of the cross-sections of the serpentine nozzle

the velocity gradient and the thinner the thermal boundary layer. Therefore, the heat flux distribution phenomenon of "small in the middle and large on both sides" appeared on the lower wall. Because of the vortex at the corner of the straight section of the outlet, the heat transfer was blocked at those locations, and the heat flux was relatively small.

Figure 31 shows the heat flux distribution on the peripheral wall of the cross-sections along the path. In the flux distribution on the upper wall, the acceleration of the upper wall at the first bend was the strongest, resulting in the strongest heat transfer on the *B–B* section. The *C–C* section was located in the thickened area of the boundary layer on the upper wall after the first bend, resulting in a weaker heat transfer. After entering the straight section of the outlet, the boundary layer thickened along the path, heat exchange was weakened, and heat flux was reduced. However, compared with the *C–C* section, the *D–D* and *E–E* cross-sections had a higher velocity gradient, which led to a stronger heat exchange. Therefore, on the upper inner wall, the heat flux of the *B–B* cross-section was the largest, while that of the *C–C* cross-section was the smallest. The *D–D* cross-section heat flux of the *D–D* cross-section was similar to that of the *E–E* cross section.

From the heat flux distribution of the lower wall surface in Fig. 31, cross section *B–B* was at the first bend. Compared with the other positions, the velocity gradient of this section was the lowest, and the heat exchange was the weakest. The *C–C* cross-section was close to the second bend, and the heat exchange was the strongest. The *D–D* and *E–E* cross-sections were in the linear section of the outlet. After the second bend, the boundary layer began to thicken, and heat transfer gradually weakened. Therefore, the heat flux was the largest in the *C–C* cross-

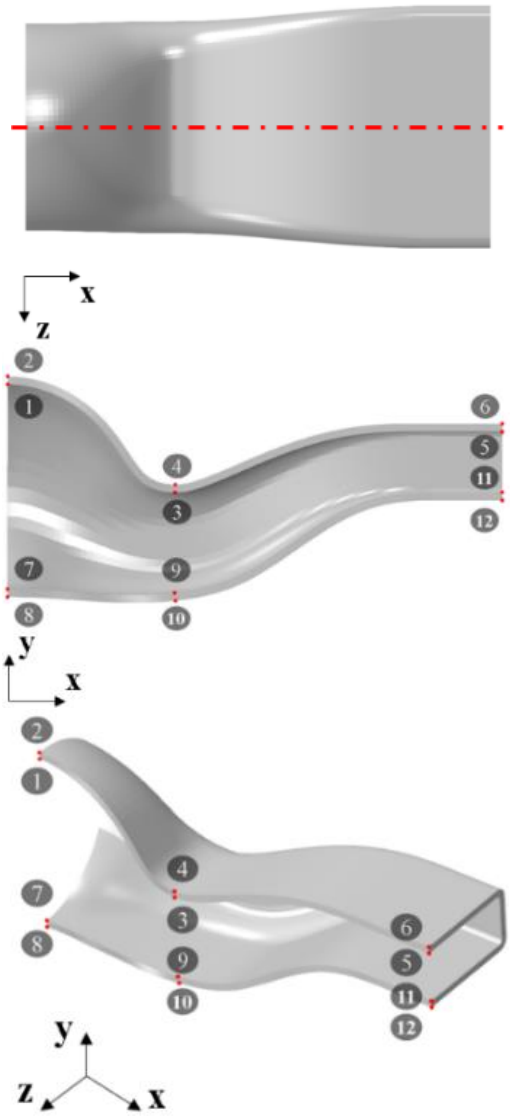

Fig. 32 Positions of feature points.

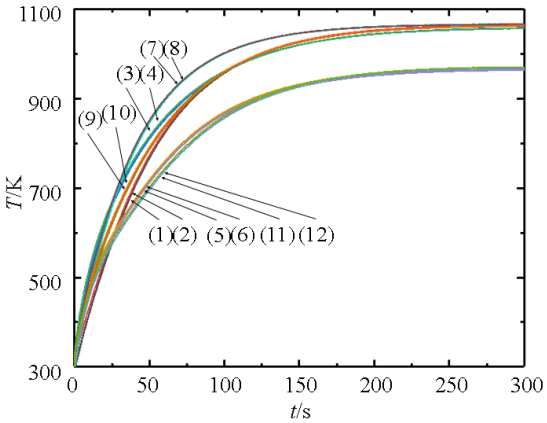

Fig. 33 Time evolutions of temperature at feature points

section, which was greater than the corresponding heat flux of the *D–D* section. The heat flux of the *D–D* section was close to that of the *E–E* section, whereas the *B–B* section exhibited the smallest heat flux.

In *B–B* section, the overall heat flux distribution on the peripheral wall gradually increased. This is because

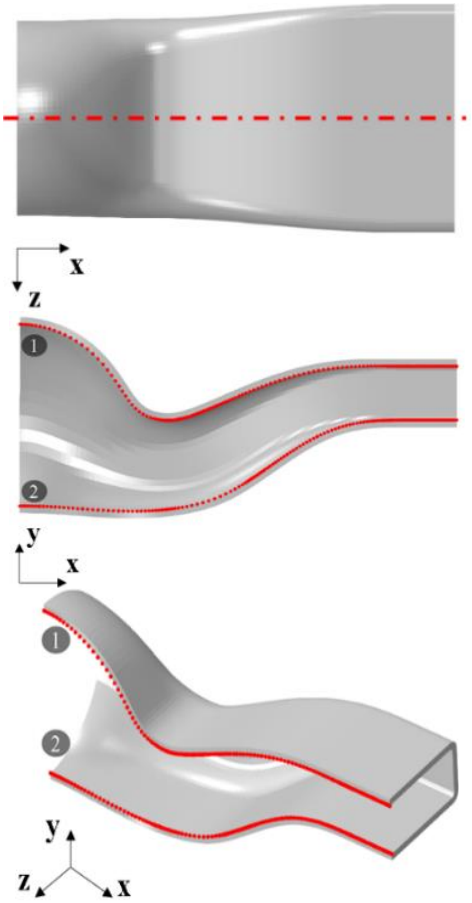

Fig. 34 Positions of the upper and lower wall symmetrical surfaces of the inner wall

the overall trend of the airflow velocity near the wall increased along the peripheral direction. Therefore, the heat exchange was continuously enhanced. There is a local heat flux valley on the peripheral wall of the *C–C* section, and the wall heat flux distribution also has a light blue area at this position, as depicted in Fig. 30. Because there were some secondary flow vortexes in the straight section of the outlet, many local peaks and valleys were generated in the *D–D* section and *E–E* sections, as shown in Fig. 31.

3.6 Structural Response Analysis

After obtaining the steady-state heat flux field, a thermal-solid coupling analysis of the serpentine nozzle was performed. Figure 32 shows the symmetrical surface of the serpentine nozzle (excluding the straight section of the nozzle inlet) and the locations of the selected feature points, including four points (1, 2, 7, and 8) on the inner and outer walls of the inlet end, four points on the inner and outer walls of the first bend (3, 4, 9, and 10), and four points on the inner and outer walls of the outlet (5, 6, 11, and 12). Comparing the temperature distributions of the feature points, the temperature distributions of the adjacent inner- and outer-wall feature points were essentially the same, as shown in Fig. 33, where the temperature distributions of the two adjacent points overlapped. In addition, the temperature stabilised towards the end of the period. Therefore, it can be inferred that when the simulation time is sufficiently long, each feature point will reach an equilibrium state.

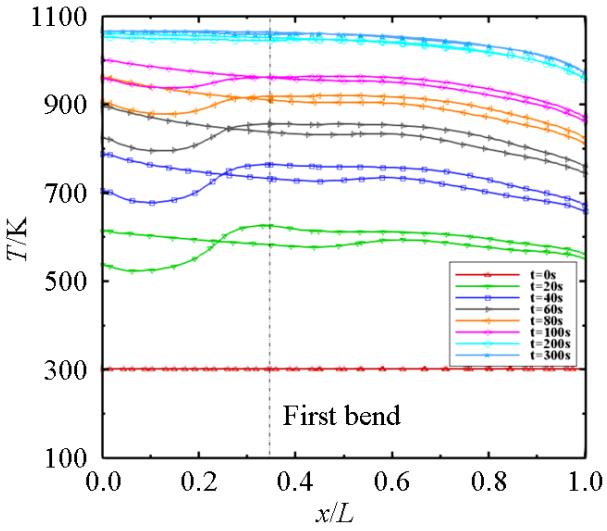

Fig. 35 Temperature distributions of the symmetry surfaces of the inner wall at different times

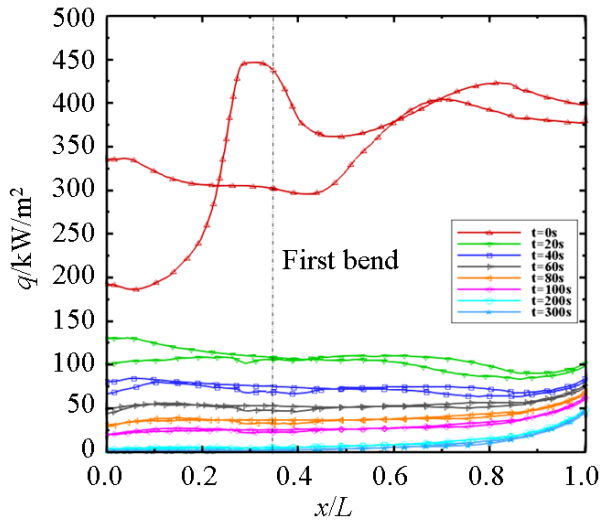

Fig. 36 Heat flux distributions of the symmetry surfaces of the inner wall at different times

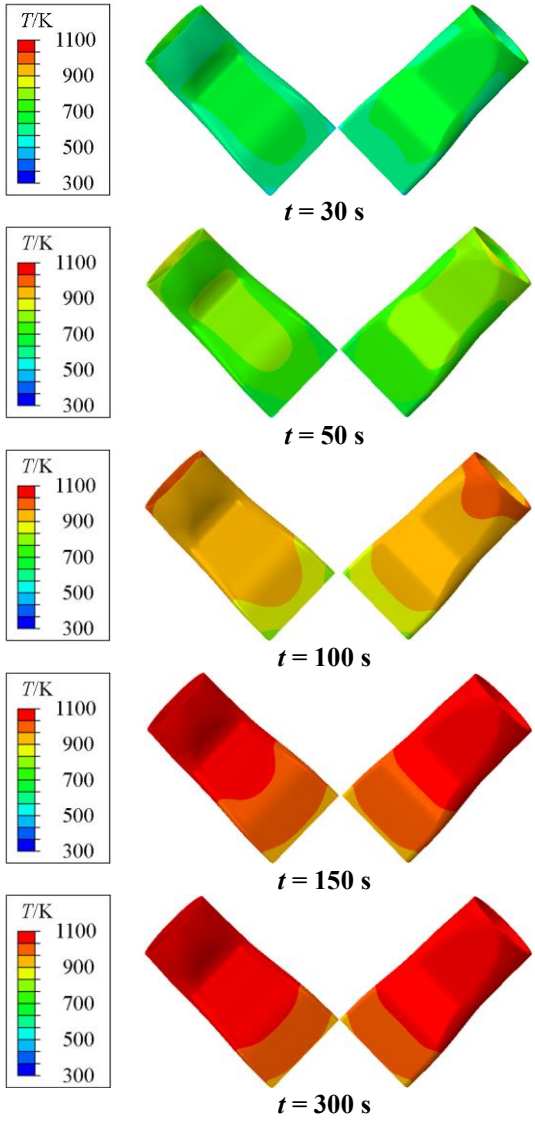

Fig. 37 Temperature distributions of the serpentine nozzle at different times

To understand the interaction between the aerodynamic heating of the flow field and the structural response more accurately. Figure 34 shows a schematic of the positions of the upper and lower symmetrical surfaces of the inner wall. Figures 35 and 36 show the time evolutions of the temperature and heat flux of the symmetrical surface of the inner wall, respectively. As time progressed, the temperature increased, but the rate of increase decreased, whereas the heat flux decreased; however, the rate also decreased. This is because under the action of aerodynamic heating, the wall temperature was the lowest at the beginning, and the heat flux was the largest. Consequently, the temperature of the structural field increased rapidly after the start of the coupling analysis. The temperature of the coupling wall surface of the structural field was transferred by MpCCI to the flow field as the new wall temperature. The temperature gradient at the flow-field wall decreased significantly, which in turn markedly reduced the heat flux. Consequently, the heat transferred to the structural field was rapidly reduced, and the rate of temperature increase of the structure wall decreased. During the initial stage, the heat flux decreased most significantly. At $t = 20$ s, the heat fluxes of the upper and lower walls almost overlapped, as shown in Fig. 36. It can be concluded that to predict the thermal load of a structure accurately, it is necessary to conduct a thermal-solid coupling analysis.

Figure 37 shows the temperature distribution of the nozzle at different times. The overall temperature distribution trend of the nozzle did not change significantly over time. The general trend was that the temperature at the inlet was higher than that at the first bend, and the temperature at the outlet was the lowest. This conforms to the laws of physics, wherein the airflow accelerates inside the convergent nozzle and the temperature of the airflow itself is constantly decreasing. Therefore, the heat flux generally decreased from the nozzle inlet to the nozzle outlet; thus, the wall temperature also decreased from the nozzle inlet to the outlet.

Over time, the high-temperature area of the serpentine nozzle continued to spread from the inlet to the outlet. The longitudinal (y direction) curvature of the serpentine nozzle exceeded the lateral(z direction) curvature. Therefore, the longitudinal heat exchange effect

was stronger than the lateral heat exchange, such that the wall temperatures of the upper and lower sides were higher than the temperature of the sidewall.

Some positions, including the upper wall of the first bend, upper wall of the second S passage, straight section of the outlet, and outlet, had higher stress than the area around them, as shown in Fig. 38. This is because the curvatures of the structure at these locations are greater than their surroundings and are therefore more constrained. In addition, the stress on the outlet continued to be at the location as that of the maximum stress of the structure over time.

At t = 30 s and t = 50 s, the phenomenon that the stress value at the first bend was close to the outlet during a certain period and was called the stress hotspot. After 100 s, the stress hotspot of the first bend was no longer evident.

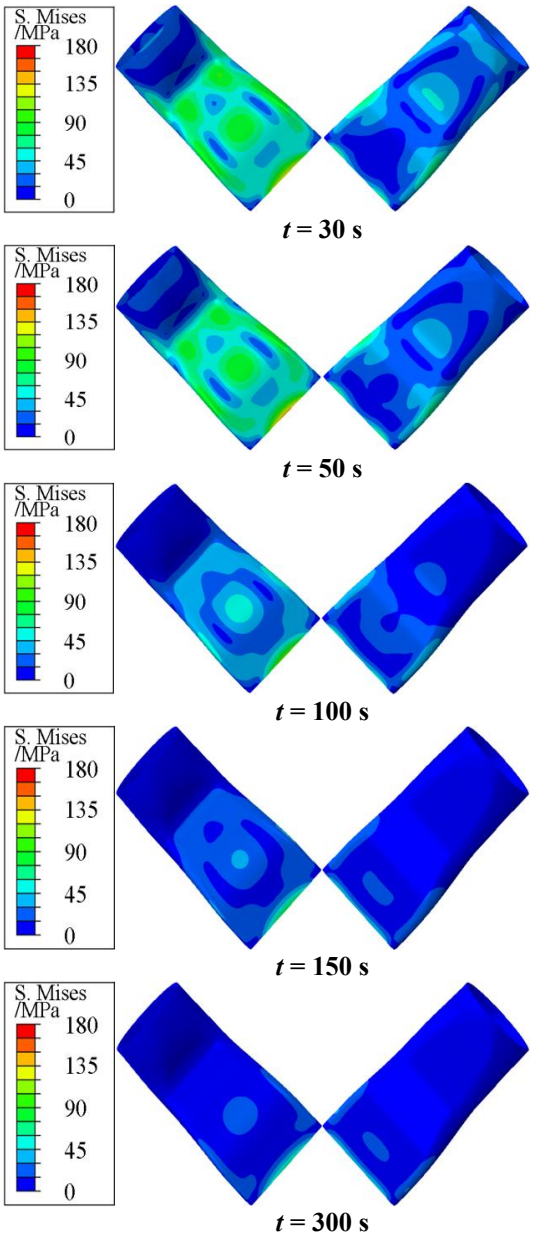

Fig. 38 Stress distributions of the serpentine nozzle at different times

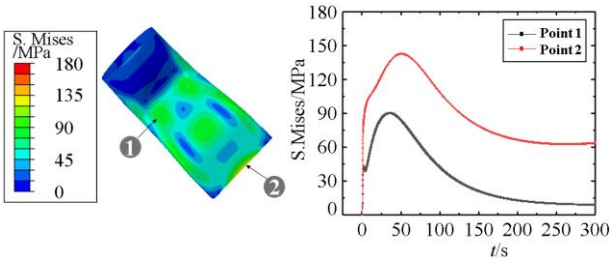

Fig. 39 Time evolutions of the stress at the positions of the stress hot spots

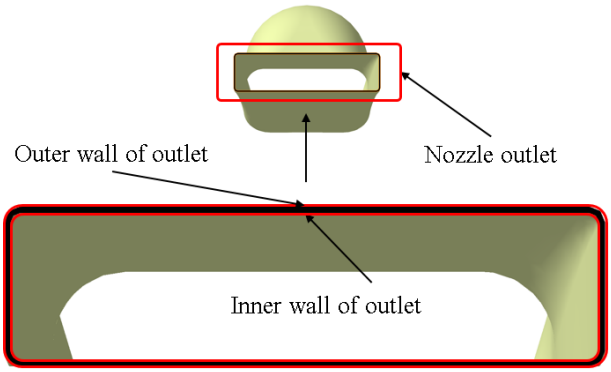

Fig. 40 The positions of the inner and outer walls at the outlet

After the beginning of calculation, two locations were named “stress hot spot”. The corresponding feature points, as presented in the left half of Fig. 39, were selected for the time-history analysis. The right half of Fig. 39 shows the time evolution of the stresses of the two corresponding local feature points. The stresses at the two feature points did not increase continuously. As time progressed, the stresses increased and then decreased with a similar trend. First, it increased sharply for a short time, and then the rate of increase decreased. After reaching a maximum value, it began to decrease slowly. This phenomenon was caused by the rapid temperature rise of the structure in the initial stage and the large temperature difference in each part, resulting in a large temperature gradient and a significant increase in stress. However, with increasing time, the heating weakened, and the rate of temperature increase decreased. This led to a decrease in the temperature gradient and the rate of stress increase until the maximum stress value was reached. As time increased, the temperature difference between each part decreased gradually and the temperature gradient decreased, resulting in a reduction in stress. The maximum stress at the outlet was higher than that at the first bend. This is because the degree of expansion of the nozzle outlet was greater than that of the first bend, and the stress generated by its expansion was larger. The maximum stress moment at the outlet occurred later than that at the first bend. This is because the first bend was heated first. The maximum stress at the outlet was 143.494 MPa at t = 51.20 s.

The maximum stress occurred at the outlet. A schematic of the inner and outer walls at the outlet is shown in Fig. 40. Figure 41 shows the stress distribution on the inner and outer walls of the outlet at t =51.20 s and adopts a peripheral wall dimensionless coordinate system. To analyse Fig. 41 in detail, Fig. 42 shows the temperature

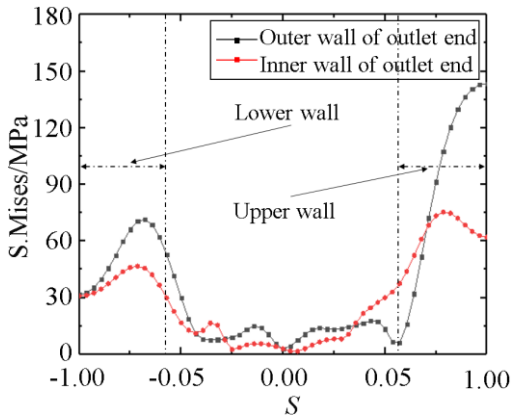

Fig. 41 Stress distributions on the inner and outer walls of the outlet at t = 51.20 s

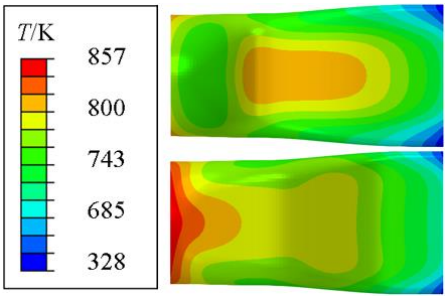

Fig. 42 Temperature distribution of the serpentine nozzle at t = 51.20 s

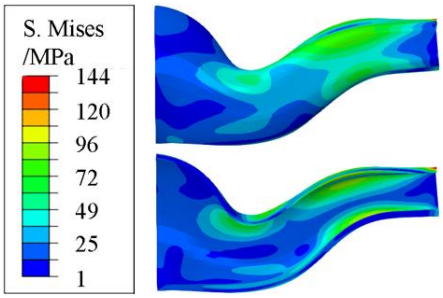

Fig. 43 Stress distribution of the serpentine nozzle after deformation at t = 51.20 s

distribution, and Fig. 43 shows the stress distribution after deformation.

As shown in Fig. 42, the closer to the outlet, the greater the temperature gradient at the upper wall than at the lower wall. Therefore, the stress distribution on the upper wall was larger than that on the lower wall. In addition, owing to the structure of the nozzle and its round-to-square structure characteristics, after slight deformation, both the upper and lower walls tended to protrude upward at the second S passage.

Because of this behaviour, the expansion of the upper wall of the outer wall of the outlet due to the thermal load was deepened. However, the expansion of the lower outer wall of the outlet and the upper and lower inner walls of the outlet decreased. Thus, a local maximum stress was generated on the upper wall of the outer wall of the outlet. Local stress minima occurred on the lower outer wall of the outlet and on the upper and lower inner walls of the outlet, as shown in Fig. 41.

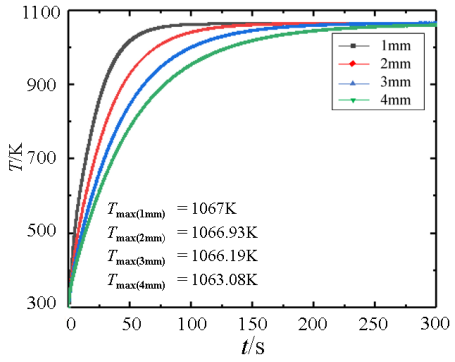

Fig. 44 Time evolutions of temperature at feature points under different wall thicknesses.

4. THERMAL-SOLID COUPLING RESPONSE OF SERPENTINE NOZZLES WITH DIFFERENT THICKNESSES

After completing the thermal-solid coupling analysis of the reference model of the serpentine nozzle with a thickness of 3 mm, the thermal-solid coupling response laws for different nozzle thicknesses were explored. For this purpose, nozzles of different thicknesses were modelled by changing the thickness of the inner wall in the outer normal direction under the condition that the aerodynamic design profile of the inner wall did not change. According to the temperature curves of the feature points over time, feature point Nos. 7 and 8 of the serpentine nozzle were the positions of the maximum temperature at the corresponding moment. In addition, the temperature curves of feature point Nos. 7 and 8 overlapped with time.

Figure 44 depicts the time evolutions of the temperature of feature point No. 7 of the nozzles with different thicknesses. As shown in Fig. 44, the temperature curves of all the feature points exhibited a similar temperature response behaviour under the aerodynamic heating of the flow field. The temperatures of all the feature points continued to increase over time until they reached a steady state. In addition, the larger the thickness of the nozzle, the smaller the heating speed because the increase in the thickness of the nozzle hindered the heat transfer of the flow field to the structure. At t = 100 s, the temperature of the serpentine nozzle with a thickness of 1 mm was close to the upper temperature limit, as shown in Fig. 44. The maximum temperature difference between nozzles with different thicknesses at t = 300 s was within 0.4%.

Figure 45 shows the temperature distribution on the symmetrical surface of the inner wall of the nozzle at different times for different wall thicknesses. Figure 45 shows the (*a*) symmetrical surface of the upper inner wall and (*b*) the symmetrical surface of the lower inner wall. As the thickness increased, the temperature gradually decreased and then increased more slowly for the same heating time. The trend of this overall distribution remained unchanged over time. During the initial stage of aerodynamic heating, the heat exchange on the upper wall at the first bend was the strongest. Local temperature extremes were observed at this location for different

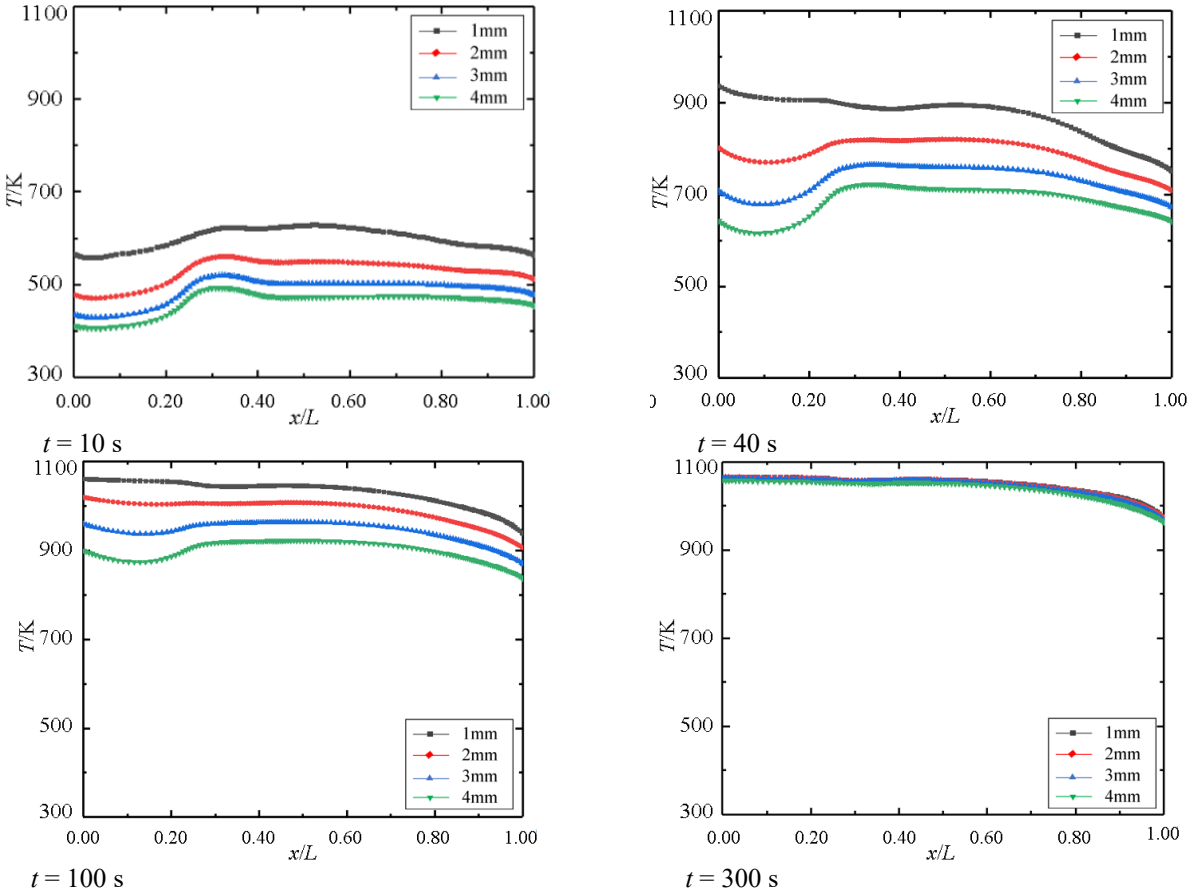

(*a*)Symmetrical surface temperature distribution of upper inner wall

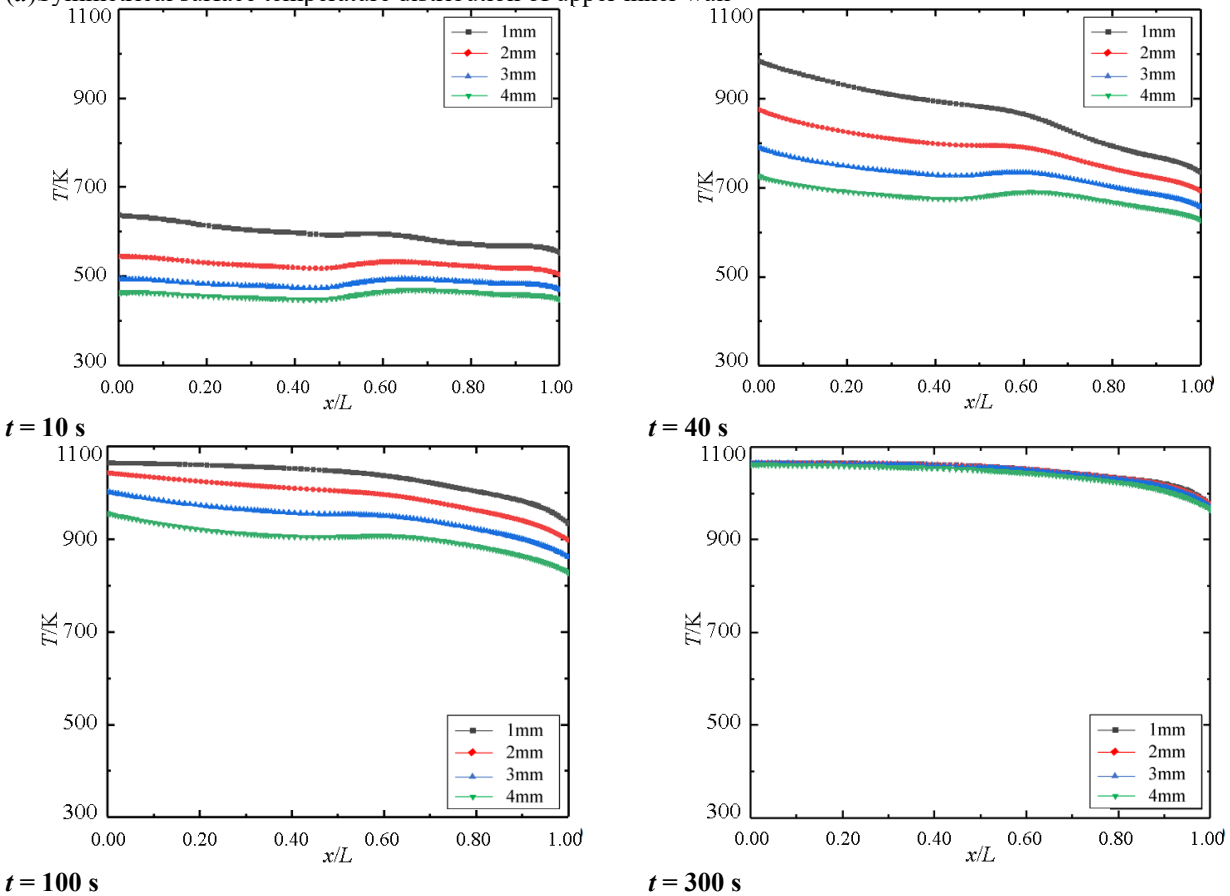

(*b*)Symmetrical surface temperature distribution of lower inner wall

Fig. 45 Temperature distributions of the upper and lower inner walls under different thicknesses at different times

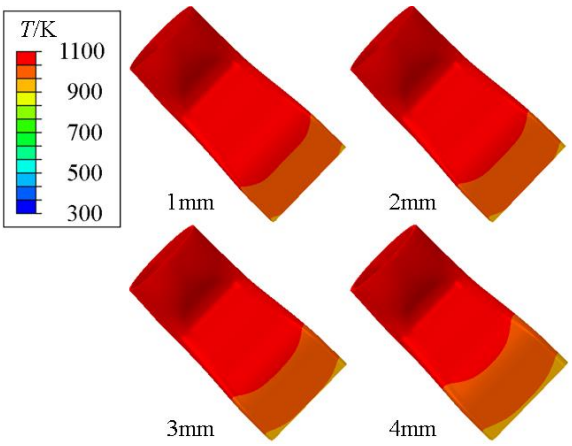

Fig. 46 Temperature distributions under different thicknesses at *t* =300 s

nozzle thicknesses. However, as aerodynamic heating at the first bend weakened, the temperature extremes were gradually transferred to the inlet. With an increase in time, this change was more obvious with the 4 mm thick nozzle. Figure 45(b) shows the local temperature extremes. This is because there was an acceleration zone at the second bend on the lower wall for each nozzle. At t = 300 s, the temperatures of the serpentine nozzles corresponding to each wall thickness were essentially the same. Figure 46 shows the temperature distributions of the serpentine nozzle for each thickness at the final moment. The temperature distributions for the nozzles with different thicknesses were similar.

The maximum stress of the serpentine nozzle with a thickness of 3 mm was observed on the outer wall of the outlet. The stress distributions on the outer wall of the outlet of the nozzles with different thicknesses at different times are shown in Fig. 47. A dimensionless coordinate system was built for the peripheral wall. Owing to the structure of the nozzle and its round-to-square structural characteristics, after deformation at the second S passage, both the upper and lower walls protruded upward. Therefore, the stress on the upper wall at the outlet was greater than that on the lower wall. In addition, the greater the thickness, the greater is the degree of expansion of the outer wall of the outlet. Hence, as the thickness of the nozzle increased, the stress on the outer wall increased. In addition, the stress on the outer wall at the outlet first increased and then decreased, whereas the stress distribution characteristics remained unchanged with time.

Figure 48 shows the stress distributions for different thicknesses of serpentine nozzles, corresponding to the moment of maximum stress. The maximum stresses for nozzles with dimensions of 1, 2, 3, and 4 mm were 54.32, 51.44, 51.20, and 51.84 s, respectively. It can be observed that the moments of maximum stress are extremely near each other. Without any support constraints around the nozzle, it underwent complete thermal expansion. The greater the thickness, the higher the degree of expansion of the outer wall, degree of stretching, and stress. Figure 49 shows the stress distributions on the outer wall of the nozzle outlet for different thicknesses. The maximum stresses corresponding to the nozzles of 1, 2, 3, and 4 mm were 86.123, 113.593, 143.494, and 165.845 MPa,

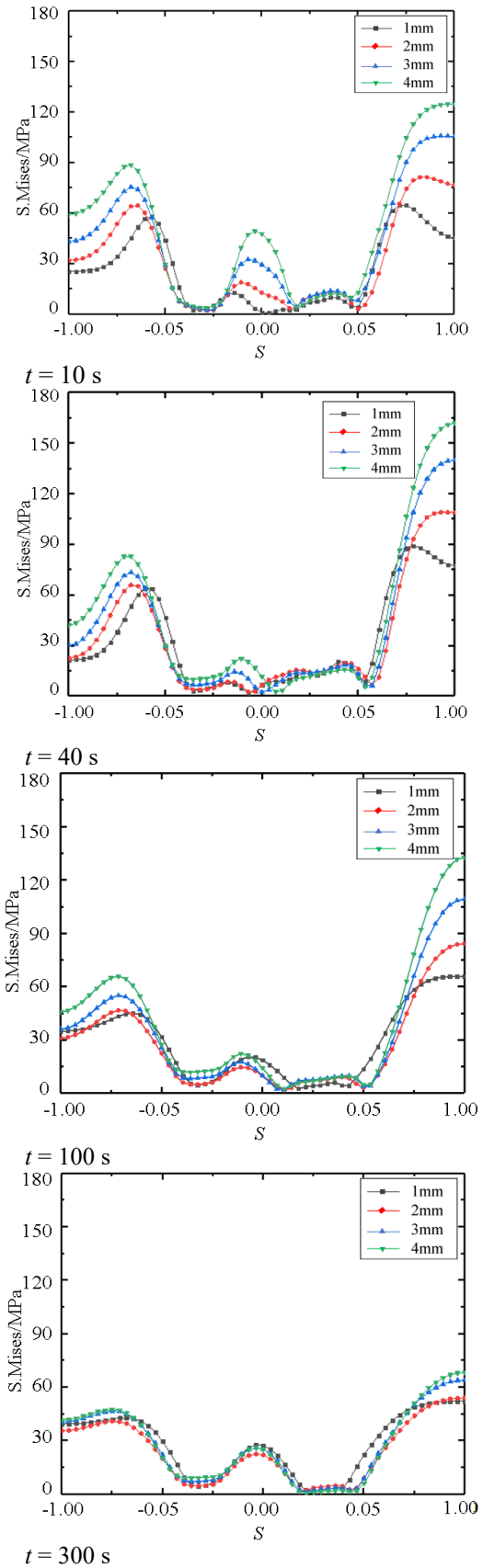

Fig. 47 Stress distributions on the outer wall of the outlet under different thicknesses at different times

respectively. This indicates that the maximum stress increases with increasing thickness, and the maximum stress at 4 mm increased by 93% compared to the maximum stress at 1 mm.

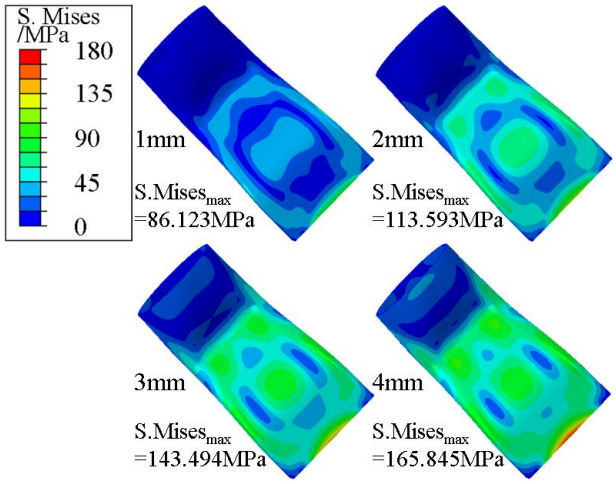

Fig. 48 Stress distributions under different thicknesses at the moments of stress maximum

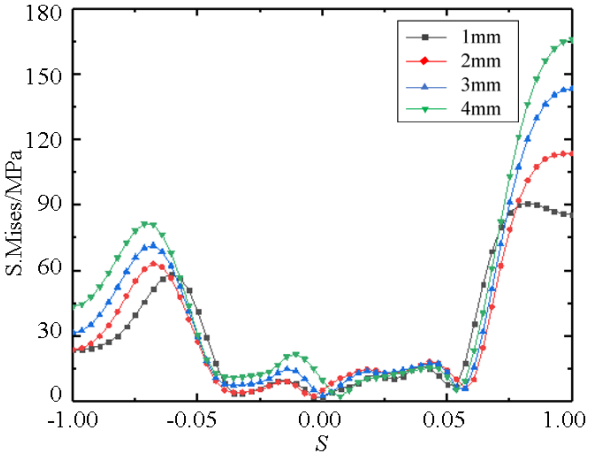

Fig. 49 Stress distributions on the outer wall of the outlet with different thicknesses at the moments of stress maximum

5. CONCLUSIONS

Based on the thermal–solid coupling method, the thermal–solid interaction response and parameter response laws for the serpentine nozzle were studied. The conclusions are as follows:

1. In the initial steady-state flow field, the overall heat flux distribution of the nozzle was non-uniform under the bent configuration. The heat transfer was the strongest at the upper wall of the first bend, and the heat flux was the highest. In addition, vortices were formed at the corner of the straight section of the outlet, which inhibited heat transfer. Thus, these locations had lower heat fluxes than their surroundings.

2. Extreme values of temperature were generated at the upper wall of the first bend and the lower wall of the second bend, and these temperatures shifted to the inlet as time increased. The overall stress distribution was not uniform; the stress first increased and then decreased with time. Stress hotspots appeared on the upper wall of the first bend and outlet. The stress hotspot at the first bend disappeared at approximately t = 100 s while the stress hotspot at the outlet was remained throughout. The structural characteristics of the nozzle caused the upper and lower walls of the second S passage to protrude upward, which increased the expansion degree of the upper wall at the outlet under the action of thermal load, and the stress at this point was the largest. The maximum stress at the nozzle was 143.494 MPa at t = 51.2 s.

3. During the analysis of the parametric law of thickness, the temperature of the serpentine nozzle gradually decreased with increasing thickness. Temperature extremes were observed in the upper wall at the first bend and in the lower wall at the second bend for each nozzle thickness. As the thickness increased, the temperature extremes became more pronounced. At the outlet, the stress distributions on the outer walls of nozzles with different thicknesses were similar. The stress increased with increasing thickness. The times of maximum stress for nozzles with thicknesses of 1–4 mm were 54.32, 51.44, 51.20, and 51.84 s. The maximum stresses corresponding to the 1–4 mm nozzles were 86.123, 113.593, 143.494, and 165.845 MPa, respectively. This indicates that at approximately t = 50 s, the nozzles generate stress maxima, and the maximum increased by 93% compared to the minimum.

4. Owing to the software limitations, we used a structured grid for the flow field when performing the meshing. This behaviour implies that if structural deformation needs to be considered, the software cannot transfer the deformation data owing to the structural grid and requires unstructured meshing of the flow field. It is also considered that, owing to the deformation, the error in the calculation of the heat flux near the wall surface increases. Therefore, the calculation method used in this study is not applicable for simulating deformation.

ACKNOWLEDGMENTS

The authors would like to express their gratitude for the financial support from the National Natural Science Foundation of China (Nos. 51876176, 52076180, and 51906204) and the National Science and Technology Major Project (J2019-II-0015-0036).

CONFLICT OF INTEREST

All authors disclosed no relevant relationships.

AUTHOR CONTRIBUTIONS

The contributions of the authors are as follows: **Jing Li Cheng**: Method design; Method Validation; Formal analysis; Data Curation; Writing - Original Draft; Writing - Review & Editing; Visualization. **Sheng Huang**: Formal analysis; Review & Editing; Supervision; Funding acquisition. **Li Zhou**: Review & Editing; Supervision; Funding acquisition. **Zhan Xue**: Wang: Review & Editing; Supervision; Funding acquisition.

REFERENCES

An, C. H., Kang, D. W., Baek, S. T., & Myong, R. S. (2016). Analysis of plume infrared signatures of S-shaped nozzle configurations of aerial vehicle. *Journal of Aircraft,* 53(6), 1768-1778. https://doi.org/10.2514/1.C033685

Arif, I., Masud, J., & Shah, I. (2018). Computational analysis of integrated engine exhaust nozzle on a supersonic fighter aircraft. *Journal of Applied Fluid Mechanics,* 11(6), 1511-1520. https://doi.org/10.29252/jafm.11.06.28989

Billig, F. S. (1967). Shock-Wave shapes around spherical and Cylindrical-Nosed bodies, *Journal of Spacecraft and Rockets,* 4(6), 822-823. https://doi.org/10.2514/3.28969

Buchlin, J. M. (2010). Convective heat transfer and infrared thermography (IRTh). *Journal of Applied Fluid Mechanics,* 3(1), 55-62. https://doi.org/10.36884/jafm.3.01.11879

Cao, Q., Li, J. X., Tang, J. L., Feng, X. P., & Hou, X. (2009). SRM ignition instantaneous fluid-solid coupling research status and development exploration. *World Science and Technology Research and Development,* 31(5), 879-883. https://doi.org/10.16507/j.issn.1006-6055.2009.05.034

Cheng, W. (2018). *Infrared signature prediction and optimization design method for serpentine nozzle*. [Ph.D. thesis, the Northwestern Polytechnical University]. Xi'an, China. https://doi.org/10.27406/d.cnki.gxbgu.2019.000473

Crowe, D. S., & Martin, C. L. Jr. (2015, January). *Effect of geometry on exit temperature from serpentine exhaust nozzles.* 53rd AIAA Aerospace Sciences Meeting. AIAA 2015-1670. https://doi.org/10.2514/6.2015-1670

Deaton, J. D., & Beran, P. S. (2016, June). *On the trade-off between stress and dynamic responses in the design of thermal structures.* 17th AIAA/ISSMO Multidisciplinary Analysis and Optimization Conference. AIAA 2016-4120. https://doi.org/10.2514/6.2016-4120

Deaton, J. D., & Grandhi, R. V. (2010, September). *Thermal-Structural analysis of engine exhaust-washed structures.* 13th AIAA/ISSMO Multidisciplinary Analysis Optimization Conference. AIAA 2010-9236. https://doi.org/10.2514/6.2010-9236

Deaton, J. D., & Grandhi, R. V. (2011, April). *Thermal-structural design and optimization of engine exhaust-washed structures.* 52nd AIAA/ASME/ASCE/AHS/ASC Structures, Structural Dynamics and Materials Conference. AIAA 2011-1903. https://doi.org/10.2514/6.2011-1903

Deaton, J. D., & Grandhi, R. V. (2012, September). *Design of engine exhaust-washed structures for an efficient supersonic air vehicle mdo application*. 12th AIAA Aviation Technology, Integration, and Operations (ATIO) Conference and 14th AIAA/ISSMO Multidisciplinary Analysis and Optimization Conference. AIAA 2012-5493. https://doi.org/10.2514/6.2012-5493

Deaton, J. D., & Grandhi, R. V. (2015, January). *Significance of geometric nonlinearity in the design of thermally loaded structures*. *56th AIAA/ASCE/AHS/ASC Structures, Structural Dynamics, and Materials Conference. AIAA 2015-*1431. https://doi.org/10.2514/6.2015-1431

Dechaumphai, P., Thornton, E. A., & Wieting, A. R. (1989). Flow-Thermal-Structural study of aerodynamically heated leading edges. *Journal of Spacecraft and Rockets,* 26(4), 201-209. https://doi.org/10.2514/3.26055

Dechaumphai, P., Wieting, A. R., & Thornton, E. A. (1988, April). *Flow-thermal-structural study of aerodynamically heated leading edges*. 29th Structures, Structural Dynamics and Materials Conference. AIAA 1988-2245. https://doi.org/10.2514/3.26055

Giles, M. B. (1997). Stability analysis of numerical interface conditions in fluid-structure thermal analysis. *International Journal for Numerical Methods in Fluids,* 25(8), 421-436. https://doi.org/10.1002/(SICI)1097-0363(19970830)25:4<421:AID-FLD557>3.0.CO;2-J

Guo, S., Xu, J. L., Qin, Q. H., & Gu, R. (2016). Fluid–thermal interaction investigation of spiked blunt bodies at hypersonic flight condition. *Journal of Spacecraft and Rockets*. 53(4), 629-643. https://doi.org/10.2514/1.A33370

Haney, M. A., & Grandhi, R. V. (2009). Consequences of material addition for a beam strip in a thermal environment. *AIAA Journal,* 47(4), 1026-1034. https://doi.org/10.2514/1.41205

Harloff, G. J., Debonis, J. R., Smith, C.F., & Bruns, J. E (1992). Three-dimensional compressible turbulent computations for a nondiffusing S-duct. *NASA Contractor Report,* 4391. https://ntrs.nasa.gov/citations/19920022996

Kamali, S., Mavriplis, D. J., & Anderson, E. M. (2020, January). *Development and validation of a High-Fidelity Aero-Thermo-Elastic analysis capability.* AIAA Scitech 2020 Forum, AIAA 2020-1449. https://doi.org/10.2514/6.2020-1449

Lee, C. C., & Boedicker, C. (1985, October). *Subsonic diffuser design and performance for advanced fighter aircraft. aircraft design systems and operations meeting.* AIAA 1985-3073. https://doi.org/10.2514/6.1985-3073

Li, Q. L., Zhou, L., Sun, P., Shi, J. W., & Wang, Z. X. (2023). Investigation on influence mechanism of aspect ratio on fluid-structure interaction

characteristic of serpentine nozzle. *Acta Aeronautica et Astronautica Sinica* 44: 628204. https://doi.org/10.7527/S1000-6893.2022.28204

Liou, M. S. (2001, June). *Ten years in the making ausm family.* 15th AIAA Computational Fluid Dynamics Conference. AIAA 2001-2521. https://doi.org/10.2514/6.2001-2521

Luo, P., & Zheng, M. (2016). Thermal-Fluid-Solid coupling analysis of aero-engine nozzle. *Journal of Aerospace Science and Technology,* 4(4), 85-95. https://doi.org/10.12677/JAST.2016.44011

Miau, J. J., Lin, S. A., Chou, J. H., Wei, C. Y., & Lin, C. K. (1988, July). *An experimental study of flow in a circular-rectangular transition duct.* 24th Joint Propulsion Conference. AIAA 1988-3029. https://doi.org/10.2514/6.1988-3029

Nigam, N., Ayyalasomayajula, S. K., Tang, Y. Y., Urbanczyk, P. S., & Alonso, J. J. (2017, June). *Design optimization of advanced exhaust systems.* 18th AIAA/ISSMO Multidisciplinary Analysis and Optimization Conference. 2017. AIAA 2017-3331. https://doi.org/10.2514/6.2017-3331

Pan, S. (2010). *Hypersonic Aerodynamic Thermal Numerical Simulation method and Large-scale Parallel Computing Research* [Ph.D. thesis, the National University of Defense Technology]. Changsha, China.

Reichert, B. A., & Hingst, W. R. (1991, January). *An experimental comparison of nonswirling and swirling flow in a circular-to-rectangular transition duct.* 29th Aerospace Sciences Meeting. AIAA 1991-0342. https://doi.org/10.2514/6.1991-342

Smith, J., & Dalenbring, M. (2006). *Aeroelastic simulation Of S-duct dynamics using structure-coupled CFD*. 25th Congress of the International Council of the Aeronautical Sciences.

Song, F., Zhou, L., Shi, J. W., & Wang, Z. X. (2021). Investigation on flow characteristics and parameters optimization of a new concept of TC nozzle. *Journal of Applied Fluid Mechanics,* 14(3), 819-832. https://doi.org/10.47176/jafm.14.03.31908

Sun, P., Zhou, L., Wang, Z. X., & Shi, J.W. (2022). Fluid-structure interaction characteristic of double serpentine nozzle. *Journal of Propulsion Technology,* 43(10), 158-167. https://doi.org/10.13675/j.cnki.tjjs.210349

Sun, X. L (2018). *Investigation on design method and performance estimation of low observable S-shaped nozzle* [Ph.D. thesis, the Northwestern Polytechnical University]. Xi'an, China. https://doi.org/10.27406/d.cnki.gxbgu.2018.000041

Sun, X. L., Wang, Z. X., Zhou, L., Shi, J. W., & Zhang, Y. C. (2015). Research on the design method of serpentine stealth nozzle based on multi-parameter coupling. *Journal of Engineering Thermophysics,* 36(11), 2371-2375.

Thillaikumar, T., Bhale, P., & Kaushik, M. (2020). Experimental investigations on the strut controlled thrust vectoring of a supersonic nozzle. *Journal of Applied Fluid Mechanics,* 13(4), 1223-1232. https://doi.org/10.36884/jafm.13.04.31069

Urbanczyk, P. S., Alonso, J. J., Nigam, N., Qi, X., & Chen, P. (2017, January). *Coupled multiphysics analysis for design of advanced exhaust systems.* 58th AIAA/ASCE/AHS/ASC Structures, Structural Dynamics, and Materials Conference. AIAA 2017-0799. https://doi.org/10.2514/6.2017-0799

Wang, W. J., Zhou, L., Wang, Z. X., & Shi, J. W. (2020). Influence of geometric parameters on overall performance of high bypass ratio turbofan nacelle and exhaust system. *Journal of Applied Fluid Mechanics,* 13(6), 1959-1973. https://doi.org/10.47176/jafm.13.06.31265

Wieting, A. R. (1987). Experimental study of shock wave interference heating on a cylindrical leading edge. *NASA Technical Memorandum,* 100484. https://ntrs.nasa.gov/citations/19870017721

Zope, A. D., Schemmel, A., Bhatia, M., Bhushan, S., & Collins, E. (2020, June). *Development and Validation of Fluid-Thermal Interaction Solver for High Fidelity Transient Simulations.* AIAA Aviation 2020 Forum. AIAA 2020-3006. https://doi.org/10.2514/6.2020-3006